

**Final Report**

**"INTRODUCTION OF NOVEL RHEOLOGICAL EVALUATION TECHNIQUES  
AND PROCESSABILITY ANALYSES TO CONTINUOUS PROPELLANT  
MANUFACTURING OPERATIONS"**

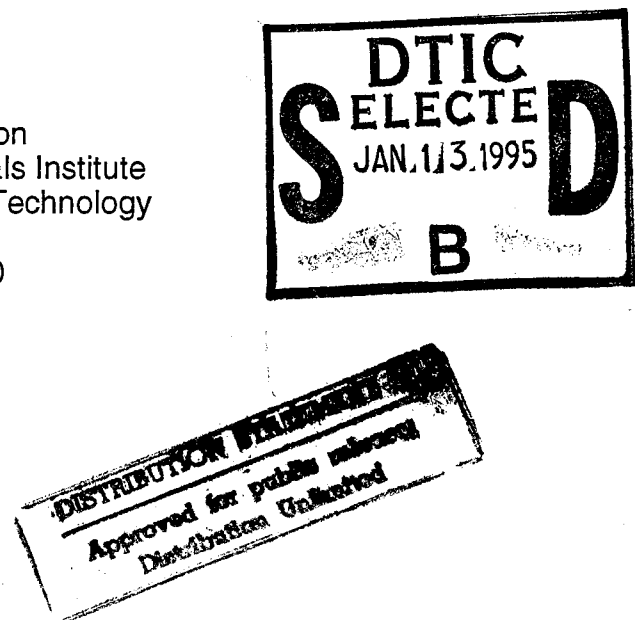
[July 14, 1990 to July 15, 1993]  
[N00014-90-J-40019]

To: Dr. Richard S. Miller, ONR  
Office of Naval Research  
800 N. Quincy St. Arlington, VA 22217

From: Prof. Dilhan M. Kalyon  
Highly Filled Materials Institute  
Stevens Institute of Technology  
Castle Point  
Hoboken, NJ 07030

Date: Nov. 28, 1993

cc. Mr. David F. Fair  
Production Base Modernization Activity  
Picatinny Arsenal, U.S. Army Base  
Dover, NJ 07801



DTIC QUADRUPOLE DRAFT

19950112 015

## **Table of Contents**

**I. Introduction: Objectives of the Project**

**II. Results**

**III. Conclusions and Acknowledgments**

**IV. Appendices**

<b>Accession For</b>	
NTIS GRA&I	<input checked="" type="checkbox"/>
DTIC TAB	<input type="checkbox"/>
Unannounced	<input type="checkbox"/>
<b>Justification</b>	
By <i>per letter</i>	
<b>Distribution</b>	
<b>Availability Codes</b>	
<b>Dist</b>	Avail and/or Special
<i>A-1</i>	

## I. INTRODUCTION

In a proposal entitled "Introduction of Novel Rheological Evaluation Techniques and Processability Analyses to Continuous Propellant Manufacturing Operations," the following tasks were proposed to PBMA :

- 1) Engineering analyses which encompassed the services related to the implementation of Stevens rheometer (designed and built at Stevens and currently on-loan to NSWC/Indian Head) and various aspects of processing at Thiokol for PBMA defined tasks.
- 2) Survey of devices and techniques to determine the particle size distribution of solid ingredients of propellants.
- 3) Development of maximum packing fraction as a tool of analysis and quality control.
- 4) Evaluation of the particle segregation problem for continuous feeding of the solid ingredients at Thiokol.
- 5) Application of various on-line monitoring techniques at Thiokol and evaluation of strategies for process control.

During the course of the year, various aspects of the program were modified following the requests of PBMA and under the management of ONR. The accomplishments and the deliverables were the following:

## II. RESULTS:

\*A new analytical model of pressurization in regular flighted screw elements, i.e., pressurization section of twin screw extruder, was developed. This analytical model allows simplified calculations for design and selection of twin screw extruder sections to be made. The developed analytical model provides design expressions involving production rate versus pressurization rate and viscous energy dissipation given the screw geometry, material properties, and operating conditions. Detailed distributions of velocity and stress are also obtained. The model accommodates the use of different slip parameters at barrel and screw surfaces. Copies of the papers are included in the Appendix.

- The analytical model developed for the enhancing of the design and screw evaluation efforts of Thiokol was incorporated into a user friendly source code for Thiokol's use and was shipped to Thiokol. The program was written in FORTRAN and interfaced into a VISUAL BASIC based source code. The source code was prepared for the IBM/WINDOWS platform for easy implementation by Thiokol. The source code can be run without the need to understand programming or modeling and can be used by technicians.
- A model and computer program (again in FORTRAN plus VISUAL BASIC) were prepared for the determination of the maximum packing fraction of solid ingredients. This source code is to be used to pinpoint detrimental changes in the particle size distributions of the solid ingredients of propellants, which will adversely affect their processability and the ultimate quality of the propellant. The source code was prepared to run on IBM/WINDOWS platform and is very user friendly. The source code was delivered to Thiokol.

- A new apparatus was built at Stevens for the experimental determination of the maximum packing fraction. This device gives a second capability to PBMA and its contractors in this area and can be used (if modified) for the day-to-day quality control of incoming solid ingredients.
- A new research and quality control apparatus with sample ports was built at SIT to analyze quantitatively the segregation of powders according to their sizes upon vibration (as might occur in continuous feeding). This device was used to document the segregation problems in continuous processing especially the segregation of melamine formaldehyde simulant powders. A copy of a paper which summarizes the results is included in the Appendix.
- A new x-ray based technique was developed and proven at SIT for the characterization of the particle size distribution of powders. This novel technique is ideal for on-line process control and can be implemented (if adapted for such use) to Thiokol operations for on-line process control of incoming powder feed. A final report was submitted on June 18, 1993.
- A new technique developed earlier to study the degree of mixing of the ingredients of highly filled suspensions (applicable to propellants) was applied to determine the degree of mixedness of samples mixed using different extrusion systems. The report, which included the analysis of samples processed using APV and W & P extruders, was delivered to PBMA on June 3, 1993.

- A report outlining the basic devolatilization guidelines which needs to be followed by Thiokol Corporation was submitted to Thiokol on February 22, 1993.
- Detailed fundamental information regarding proper selection of operating parameters in twin screw extrusion was prepared in December '92 and modified a number of times upon the input of PBMA/Mr. David Fair. This information will allow the Government/Industry and Academia to speak a common language. It also identifies major safety concerns in twin screw extrusion processing of gun propellants and should be used extensively by Thiokol.
- A report on the experimental design of LOVA XM 43 processing was submitted to Thiokol on February 4, 1993.
- A report detailing the x-ray technique developed for particle size distribution analysis and application to aluminum powders was submitted.
- Information and design analyses were provided to PBMA and its contractors on an as needed basis. These analyses included feedback on design, use of our on-line rheometer and solvent recovery. The adjustable gap rheometer invention was filed for a patent and the Government was given a non-exclusive license for its use.
- Experiments for the analysis of the segregation of melamine powders (used by Thiokol as simulants for RDX) were carried out. A report was submitted on July 20, 1993 entitled "Assessment of Segregation Effect, for Melamine Powder Subjected to Vibration". A further manuscript entitled "Effects of

Segregation on the Packing of Symmetric and Asymmetric Particles with Multimodal Particle Size Distributions was submitted to PBMA and Thiokol.

- Upon the input of PBMA, information regarding the application of goodness of mixing analysis techniques to extruded samples was given to NSWC.
- Upon the request of PBMA a crash program on the mixing and rheology of CAB based LOVA formulations was carried-out. This project was completely outside the scope of our original proposal. A comprehensive report dated June 28, 1993 was submitted to PBMA and Thiokol.

With these, all of our promised and later modified objectives are fully completed. The funds for FY 92 are completely spent by July 14, 1993.

### **III. CONCLUSIONS AND ACKNOWLEDGMENTS:**

This funding originating from the USArmy Production Base Modernization Activity (PBMA) in Picatinny Arsenal Army Base in New Jersey and managed by ONR allowed us to contribute directly to engineering analysis and design tasks associated with the PBMA and its contractor Thiokol Corporation at Longhorn, LA. The engineering analysis results were of direct benefit to Thiokol Corporation and PBMA. Various design improvements and data necessary for plant design emanated from our contributions. They should have a solid impact on the future progress of the prototype facility to produce LOVA formulations to be built by Thiokol Corporation under the sponsorship of the US Army.

The other progress reports, papers, computer programs and other design and analysis tools relevant to this project are available from Professor Dilhan M. Kalyon at Stevens Institute of Technology [201 216 8225, fax 5601]

We are very grateful to US Army and ONR for this funding which we received. We also thank our Program Managers Mr. David F. Fair of PBMA and Dr. Richard S. Miller of ONR for their diligent guidance.

## APPENDICES



To be published in next issue  
Please send corrections by  
RETURN OF MAIL

Powder Technology

798  
POWDER  
TECHNOLOGY

## Effects of segregation on the packing of spherical and nonspherical particles

Thomas J. Fiske, Sudhir B. Railkar, Dilhan M. Kalyon\*

Highly Filled Materials Institute, Department of Chemistry/Chemical Engineering, Stevens Institute of Technology, Hoboken, NJ 07030, USA

Received 10 December 1993; in revised form 27 May 1994

### Abstract

The packing of particles is important in the processing of the powders and in the ultimate properties of articles processed from the powders. Using an apparatus originally designed for the experimental determination of the packing density of powders, segregation effects with spherical and nonspherical particles with low aspect ratios were studied. The segregation of the powder samples according to particle sizes occurred upon vibration of the bed, following the well-known mechanisms of segregation according to size and elutriation segregation due to entrainment of particles in air. Segregation effects were also demonstrated with a melamine powder which consisted of nonspherical particles with low aspect ratios. Furthermore, additional data are provided for the packing density values of spherical particles with multimodal particle size distributions, which further support the theory of Ouchiyanma and Tanaka on the packing of spherical particles, when segregation effects are not significant.

**Keywords:** Segregation; Packing

### 1. Introduction

The proper selection of the size and shape distributions of particulate materials is critical in various industries, which include ceramics, pharmaceuticals, detergents, magnetic media, batteries and propellants/explosives. The products of such large-scale industrial operations rely on the ability to tailor the size and shape distributions of solids to achieve high-density packing arrangements which maximize the amount of solids per unit volume. Various experimental and theoretical methods for the analyses of particle packing are available [1-14].

In 1930, Westman and Hugill [1] studied the packing of unimodal and bimodal spherical particles experimentally and determined the limiting cases for the maximum packing of spherical particles with a bimodal size distribution. Furnas [2] showed the dependence of the packing density on the diameter ratio of small to large particles and their fractional volumes. Scott [3] estimated the packing fraction of uniform spherical particles using cylindrical and spherical containers. Pouring of unimodal and noncohesive spherical particles into rigid containers generates a random packing frac-

tion between 0.6 and 0.64 [1-3].

McGeary [4] used experimental and visual techniques to study the packing of spherical particles in cylindrical tubes, using both binary and ternary mixtures of particle sizes. For binary mixtures for which the ratio of particle diameters exceeded 7, the maximum packing fraction values were around 0.8. Below a particle diameter ratio of 7, the maximum packing fraction decreased significantly. Debbas and Rumpf [5] treated spherical solid particles and voids as two components in the packing process and studied the packing of various particulates with broad size distributions.

Ouchiyanma and Tanaka [6-8] developed a packing model to predict the packing densities of spherical particles. Starting with the number of contacts between the spherical particles and the porosity, a simplified relationship between the maximum packing fraction and the particle size distributions of spherical particles was derived. This relationship was verified experimentally [6].

Gupta and Seshadri [9] used the packing model of Ouchiyanma and Tanaka [7] and the experimental data on suspension rheology generated by Chong et al. [10] to show the accuracy of the theory proposed by Ouchiyanma and Tanaka [6-8]. Poslinski et al. [11] applied the maximum packing fraction model of Ouchiyanma

\*Author for correspondence.

and Tanaka [6-8] to glass spheres with bimodal size distributions. It is also possible to predict the packing fractions via the Monte Carlo numerical simulation techniques as obtained by Visscher et al. [12]. The packing of asymmetric particles such as rods and spheres has also been studied [13].

Large-scale industrial operations involving particulate solids depend on various solids handling techniques, including flow through bins and hoppers, and pneumatic conveying. In such operations when a column of solids is disturbed through vibration, shaking and stirring, gaps between particles are generated which allow smaller particles to percolate downwards [14]. Such a segregation of particles according to size and/or density may be detrimental to the quality of the product. The segregation problem was addressed by O'Brien et al. [15] using Monte Carlo simulation.

Matsumoto et al. [16], and Popplewell and Peleg [17] discuss the effects of segregation on the operation of fluidized beds and bubble columns. Alonso et al. [18] proposed a simplified analysis to generate a segregation index.

In this paper spherical and nonspherical particles with multimodal size distributions are used to investigate their packing and segregation behavior. An industrially relevant powder with particles of low aspect ratio, i.e. a melamine powder, is also included in the study.

## 2. General background

### 2.1. Packing of uniform spheres

The packing fraction of particulates,  $\phi$ , is defined as the ratio of the volume of solids to the total volume, i.e. voids plus solid. When the void volume reaches a minimum for a given system, one obtains the maximum packing fraction,  $\phi_{\max}$ . From geometric considerations, it is possible for uniform spheres to be arranged into several different packing arrays such as simple cubic, orthorhombic, tetragonal-sphenoidal and rhombohedral, which have maximum packing fractions of 0.5336, 0.6046, 0.6981 and 0.7405, respectively [4]. In the random packing of uniform spheres in cylindrical containers, simple cubic and rhombohedral arrangements of particles are unstable. In contrast, the orthorhombic and tetragonal-sphenoidal arrangements are stable [3,4]. Experimentally, the packing fraction of uniform spheres is observed to be around 0.619, indicating that indeed the orthorhombic structure is one of the predominant arrangements [4].

### 2.2. Packing of bimodal distribution of spheres

It is possible to increase  $\phi_{\max}$  beyond 0.619 by increasing the modality of the packing mixture [4-13].

For a binary mixture, the ratio of the diameter of the larger spheres to that of the small spheres,  $\alpha$ , plays an important role. For  $\alpha > 7$ , the small particles can fit easily into the interstitial spaces between the larger spheres. This increases the packing fraction. On the other hand, for  $\alpha < 7$ , the packing efficiency diminishes rapidly [4]. The maximum packing fraction is also a function of the mixing ratios (volume fraction) of the two components. Fig. 1 shows the maximum packing fractions of bimodal mixtures of spheres for various values of  $\alpha$  as a function of the volume fraction of small spheres. The curves which begin and terminate at 0.619 were generated by the packing model of Ouchiyama and Tanaka [6-8]:

$$\phi_{\max} = \frac{\sum D_i^3 f_i}{\sum (D_i \sim D_a)^3 f_i + \frac{1}{\beta} \sum [(D_i + D_a)^3 - (D_i \sim D_a)^3] f_i} \quad (1)$$

where

$$\beta = 1 + \frac{4}{13} \times \frac{\sum (D_i + D_a)^2 \left(1 - \frac{3}{8} \frac{D_a}{(D_i + D_a)}\right) f_i}{\sum (D_i^3 - (D_i \sim D_a)^3) f_i} \quad (2)$$

and

$$D_a = \sum D_i f_i \quad (3)$$

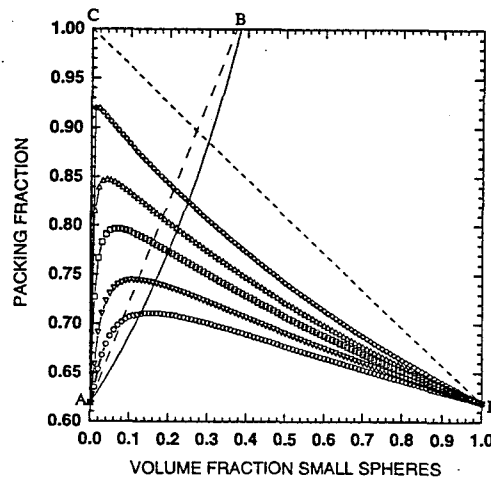


Fig. 1. Packing curves for various diameter ratios according to Ouchiyama and Tanaka [6-8] and limits provided by Westman and Hugill [1], i.e. AB and CD. (○) [6-8],  $\alpha=4$ ; ( $\nabla$ ) [6-8],  $\alpha=5$ ; ( $\square$ ) [6-8],  $\alpha=7$ ; ( $\triangle$ ) [6-8],  $\alpha=10$ ; ( $\diamond$ ) [6-8],  $\alpha=20$ ; (—), [6-8]; (---) AB; (----) CD.

In the above equations,  $\phi_{mo}$  is the maximum packing of uniform spheres,  $D_a$  is the average diameter of particles,  $D_i$  is the diameter of the  $i$ th size fraction.  $(D_i \sim D_a)$  is defined as follows [6]:

$$(D_i \sim D_a) = 0 \text{ for } D_i \leq D_a \quad (4)$$

and

$$(D_i \sim D_a) = D_i - D_a \text{ for } D_i > D_a$$

The number fraction of the  $i$ th component,  $f_i$  is defined by:

$$f_i = \frac{(v_i/D_i^3)}{\sum(f_i/D_i^3)} \quad (5)$$

where  $v_i$  is the volume fraction of the  $i$ th component in the mixture.

The solid curve with the positive slope in Fig. 1 is obtained from Eq. (18) of Ouchiyma and Tanaka [7], assuming that the porosity value obtained upon ideal packing of unimodal spheres is 0.381. It is given by:

$$\phi_m = \frac{0.619}{V_c} \quad (6)$$

Here  $V_c$  is the volume fraction of bed material. This packing equation is based on the assumption that the smaller particles completely fill the interstices of the larger particles. To verify the validity of the equations, the upper and lower limits for a binary mixture, as considered by Westman and Hugill [1], are also plotted in Fig. 1. Upon addition of smaller spheres to a bed of larger spheres, the smaller spheres are completely embedded in the interstitial space between the larger spheres and the maximum packing fraction increases, as depicted by the dashed line, AB, in Fig. 1. On the other hand, upon addition of a few large spheres to a large quantity of infinitely small spheres, the large spheres will be completely immersed in the small spheres. This situation is depicted by line CD in Fig. 1.

At low concentrations of small spheres and at high  $\alpha$  values, Eq. (1) predicts higher packing fraction values than the limits suggested by Westman and Hugill [1]. It is clear from Fig. 1 that as  $\alpha$  increases for a given volume fraction of small spheres,  $\phi_{max}$  increases. For a given  $\alpha$ , the mixing ratio of the spheres can be optimized to maximize the total solids content of the solid particles per unit volume. This maximum packing density occurs at the apex of the intersection of Eqs. (1) and (6). This apex shifts to higher concentrations of smaller spheres as  $\alpha$  increases. For any given ratio of the diameter of larger spheres to the diameter of smaller spheres, the packing behavior is represented by the curve defined by Eq. (6) up to the intersection with the curve defined by Eq. (1).

### 2.3. Segregation of bimodal system of spheres

Various handling operations for solids, i.e. the use of gravity-driven columns, drag-flow-based extruders and pneumatic systems which involve the entrainment of the particles in high-velocity air, can all generate the preferential motion of the particles according to their size, shape and density. One mode of the segregation process according to size is illustrated in Fig. 2. In this experiment, chrome-plated steel balls with a bimodal particle size distribution were placed into a vertical cylindrical column. The particle size ratio,  $\alpha$ , was 4. Upon vibration of the bed at a frequency of 7.5 Hz and with an amplitude of 1.5 cm for a duration of 30 s, the smaller spheres were seen to percolate downwards to completely force the migration of the larger spheres to the top of the column.

Another operation which generates segregation of particles according to their sizes is the pouring of a mixture of multisized particles into a heap. The finer particles percolate through the moving inclined surface of the heap while the coarser particles preferentially tumble away from the pouring point of the heap [19].

Alonso et al. [18] defined a segregation index,  $S$ , based on analysis of the free-surface segregation process:

$$S = \left( \frac{\rho}{\alpha} \right) \left[ \frac{1 + V_c(\alpha - 1)}{1 + V_c(\rho - 1)} \right] \times \left( \frac{1 - \epsilon \exp \left[ - \frac{1 - \epsilon}{\epsilon} \left\{ \left[ 1 + \frac{1}{1 + V_c(\alpha - 1)} \right]^2 - 1 \right\} \right]}{1 - \epsilon \exp \left[ - 3 \frac{1 - \epsilon}{\epsilon} \right]} \right) \quad (7)$$

where  $\rho$  is the density ratio of the large particles to that of the small particles,  $\epsilon$  is the porosity, and  $V_c$  is the volume fraction of large particles. If  $S$  is less than one, the large particles tend to behave as floaters, rising to the top of the system. On the other hand, for  $S$  greater than one, the large particles tend to sink to the bottom. If  $S$  is equal to one, segregation should not take place.

At low concentrations of large particles, Eq. (7) reduces to

$$S = \frac{\rho}{\alpha} \quad (8)$$

At high concentrations of larger particles, i.e. as  $V_c$  approaches 1, Eq. (7) indicates that the segregation index,  $S$  becomes less than one:

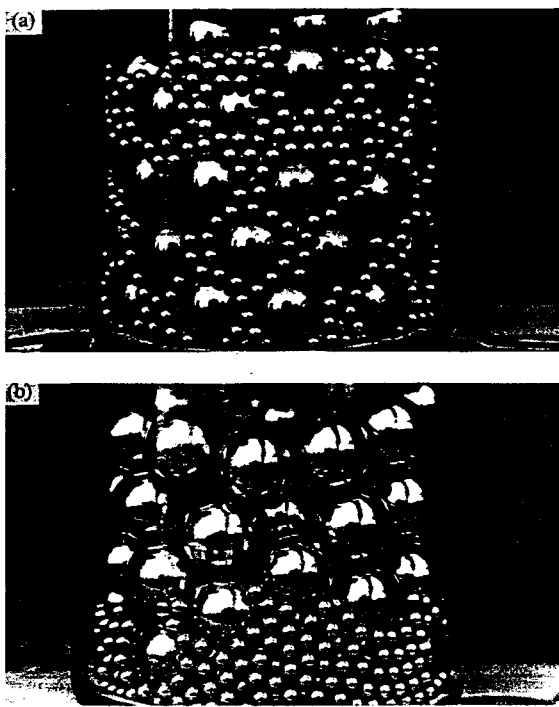


Fig. 2. Demonstration of segregation of metal spheres with  $\alpha=4$  in a transparent container.

$$S = \left( \frac{1 - \infty \exp \left[ - \frac{1-\epsilon}{\epsilon} \left\{ \left[ 1 + \frac{1}{1+V_c(\alpha-1)} \right]^2 - 1 \right\} \right]}{1 - \epsilon \exp \left[ -3 \frac{1-\epsilon}{\epsilon} \right]} \right) \quad (9)$$

Eq. (9) suggests that segregation under such conditions is principally controlled by the percolation of the smaller particles through the larger ones, regardless of the density of the larger particles.

### 3. Experimental

The packing and segregation experiments were conducted with ball bearings, glass spheres and melamine powder. Chrome-plated steel ball bearings of diameter 6.35 mm, 3.175 mm and 12.7 mm were used. These ball bearings were obtained from McMaster Carr (NJ, USA). The ball bearings had an average diameter deviation of  $\pm 2.54 \mu\text{m}$ .

Five different grades of glass particles were prepared by sieving of soda-lime glass spheres procured from Potter Industry Inc. The mean particle diameter, standard deviation and the range of the distributions are shown in Table 1.

Table 1

Mean diameter, standard deviation and range of particle sizes in the five grades of glass spheres used in the study

Material	Mean diameter ( $\mu\text{m}$ )	Standard deviation ( $\mu\text{m}$ )	Range ( $\mu\text{m}$ )
Glass #1	139	47	40-300
Glass #2	133	44	40-300
Glass #3	11	4.3	4-30
Glass #4	219	51	120-400
Glass #5	81.5	9.1	65-100



Fig. 3. SEM micrograph of the melamine powder.

Finally, a melamine powder was also used in the packing and segregation experiments. The melamine powder was in the form of nonspherical particles, with typical aspect ratios of around 2, with a standard deviation of 0.22. A scanning electron micrograph of the melamine powder is shown in Fig. 3. The equivalent diameters of the particles were obtained using the Automatix image analysis program, which determined for each particle the distances from the center of the particle to the perimeter (following the change in curvature with respect to a fixed coordinate system).

#### 3.1. Packing experiments

In order to study the packing of unimodal and bimodal glass and metal spheres, Plexiglas tubes of various diameters were used. These were connected to a sieve shaker (CE Tyler Combustion Engineering Inc.) with special adapters. The frequency and the amplitude used during the operation of the sieve shaker were 7.5 Hz and 1.5 cm, respectively.

The tubes were filled with preweighed powder to an initial height of 7 cm. The total volume of the sample under the initial loosely packed conditions was noted. The tube containing the powder was shaken at constant frequency and amplitude until the sample reached minimum height. As a second method to determine the volumes occupied by the powder and the voids, water was filled to the minimum packed height and the column was weighed. The above experimental procedure was repeated for cylindrical containers with different diameters. The packing fraction of the uniform spheres was calculated using the method of extrapolation suggested by Scott [3]. Cylindrical containers with diameters greater than 2.54 cm were large enough to eliminate the wall effect. For the glass and metal spheres, the majority of the experiments were conducted in a cylindrical container with a diameter of 5.715 cm.

### 3.2. Segregation experiments

In order to study the segregation of solid powders subject to vibration, a simple segregation apparatus was built. The apparatus consisted of a cylindrical container, which was installed on the sieve shaker, equipped with openings at different heights from the base. The arrangement facilitated the collection of specimens at different heights without disturbing the rest of the column of solid powder. The three openings in the main tube were initially kept plugged during the shaking. A sample thief was used to collect samples from the column at three different heights during the experiment. These locations were 0.02, 0.06 and 0.10 m from the base of the apparatus and are designated 'Bottom', 'Middle', and 'Top'.

In the case of glass spheres, the samples collected from these locations were sieved and analyzed to obtain the relative percentages of the size fractions which were designated as the small and large glass spheres. On the other hand, a scanning electron microscope (SEM) was used to characterize particle size distributions of the melamine samples. The samples obtained from the segregation apparatus were mounted on brass and aluminum sample holders using a double-sided conductive adhesive carbon tape. The micrographs of the powder samples were obtained at magnifications of between 200 and 7500.

## 4. Results and discussion

The maximum packing fraction values of the uniform steel balls determined according to the method of Scott [3] are summarized in Table 2. The maximum packing fractions obtained upon successive multiple trials for chrome plated steel balls with different diameters are shown in Table 2. These experimental values were

Table 2  
Packing of spheres: experiment vs. theory

Material	Mean diameter (mm)	Experimental $\phi_{max}$	Theoretical $\phi_{max}$
Steel	3.2	0.63	0.619
Steel	6.4	0.63	0.619
Steel	12.7	0.64	0.619
Glass #1	139	0.65	0.648
Glass #2	133	0.65	0.648

based on 29, 18 and 10 trials for chrome-plated steel balls with diameters of 3.175 mm, 6.35 mm and 12.7 mm respectively. The packing values obtained were within 1.5% of each other. These experimental values agree well with those reported in the literature.

The experimentally determined maximum packing fraction values of the glass spheres are also included in Table 2. Due to the fact that the glass spheres used exhibit a wide size distribution, their packing fraction values are expected to be greater than that of unimodal spheres [4]. Glass #1 exhibited an experimental maximum packing fraction of 0.65, while Glass #2 also exhibited an experimental maximum packing fraction of 0.65. From the known particle size distributions, the maximum packing fractions,  $\phi_{max}$ , were calculated on the basis of the Ouchiya and Tanaka relationship, i.e. Eq. (1), and are shown in Table 2. Good agreement between the experimental results and the Ouchiya and Tanaka model was obtained when the radius of the cylindrical containers used exceeded 2.54 cm, i.e. column diameter to particle diameter ratio was greater than 100, at which dimensions the wall effects were negligible.

The packing fraction values obtained experimentally with glass spheres which exhibited an approximate size ratio of 7 are compared with other experimental results available in the literature and with the theory of Ouchiya and Tanaka [6-8] in Fig. 4. Our experimental results are also presented in the format used for bimodal size distributions, i.e. packing fraction as a function of the volume percent of smaller spheres, for convenience. The diameter ratio,  $\alpha$  of 7 was obtained experimentally by mixing glass sample designated as #3 with #5 (Table 1) and  $\alpha$  ratio of 20 was obtained by mixing glass sample #3 with #4. The experimental data are reported in terms of 95% confidence intervals determined according to Student's t-distribution, based on three trials for each volume fraction. The experimental behavior is very well represented by the theory of Ouchiya and Tanaka [6-8]. The two-region model represented by Eqs. (1) and (6) fit the data well, indicating that indeed the behavior is represented by two separate regions. The maximum packing fraction, i.e. 0.775, occurs at a volume fraction of small spheres of 0.20.

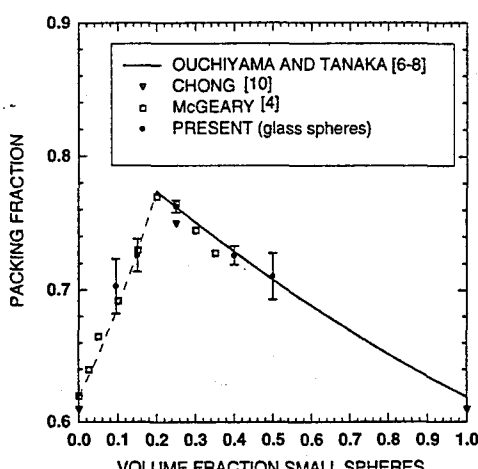


Fig. 4. Packing density of glass spheres with  $\alpha=7$ . Larger spheres from Glass #5 and smaller spheres from Glass #3.

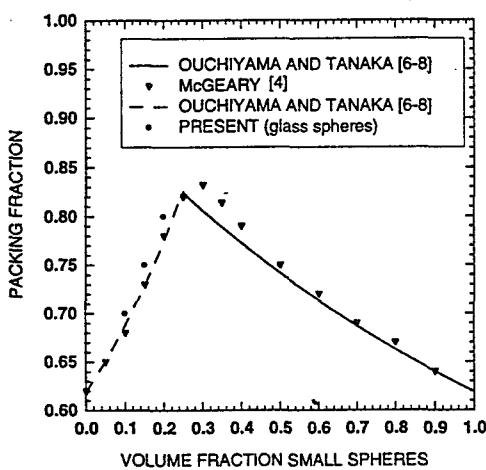


Fig. 5. Packing density of glass spheres with  $\alpha=20$ , i.e. larger spheres (Glass #4) and smaller spheres (Glass #3).

The comparisons of the experimental results obtained with glass spheres with an approximate diameter ratio of 20 with the other available experimental results and the theory of Ouchiyma and Tanaka are shown in Fig. 5. The maximum packing fraction occurs at a volume fraction of small spheres of about 0.25. The value of the maximum packing fraction for  $\alpha=20$ , i.e. 0.83, is significantly greater than that determined at  $\alpha=7$ . The experimental results for glass were obtained using five trials for each volume fraction. Due to the excellent reproducibility of the experiments, the resulting confidence intervals were too tight to appear on the plot.

The validity of the two-region model is again indicated. However, the experimental results obtained at  $\alpha=20$  do not agree with the theory of Ouchiyma and Tanaka as well as they did at the particle size ratio,  $\alpha$ , of 7.

As will be suggested in the following section, these differences are associated with particle segregation effects, which are enhanced for the greater particle size ratio of 20.

#### 4.1. Segregation

The results of the segregation experiment for the glass spheres are shown in Fig. 6 for  $\alpha=7$ . The volume percentage of small spheres as a function of location in the packing apparatus is presented. Here, the volume percent of smaller spheres represent all spheres which have diameters between 4 and 30  $\mu$  and the volume fraction of the larger spheres represents all spheres between 65 and 100  $\mu$  in diameter. For comparison purposes, the volume percentage of the small spheres of the original mixture is included. The volume percentage of larger spheres at the same locations are also given in Fig. 6.

The volume percentage of the small spheres increases from the top to the bottom upon vibration. The cylinder contains 13% of small spheres at the top, 19% at the middle, and 21% at the bottom (by volume). The large spheres make up the remainder at each location in the cylinder. The percentage of larger spheres increases from about 79% at the bottom to about 87% at the top of the cylinder. These results clearly indicate the segregation of the mixture according to size by the percolation of the small spheres through the larger

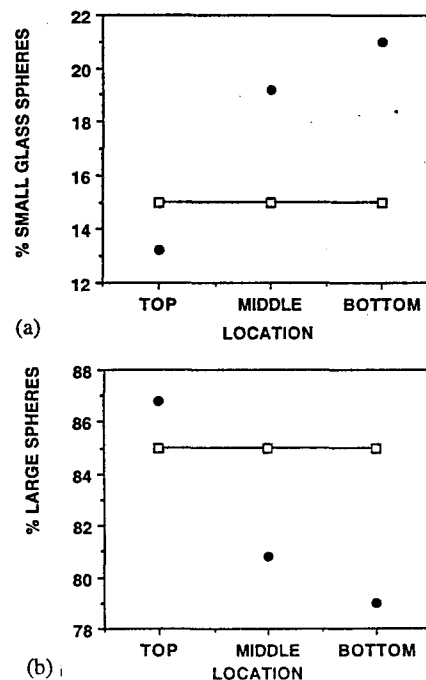


Fig. 6. Results demonstrating the segregation of a column of multimodal glass spheres upon vibration; (a) large spheres, (b) small spheres; (—□—) unsegregated, (●) segregated.

spheres.

Segregation changes the packing fraction of different layers in the column. The material found at the top portion of the tube would generate a theoretical packing fraction of 0.71. The middle portion of the cylinder generates a maximum packing fraction of 0.76, while the sample found at the bottom of the cylinder would generate a packing fraction of 0.77. These results suggest that experimental techniques designed to experimentally determine the packing density of particulates can themselves be subject to segregation effects. The segregation of particles according to size can generate zones of material with packing fractions which are very different than the expected particle density for the entire column.

Such a variation in maximum packing fraction, for example in a hopper which feeds powders into a continuous processing operation, would generate a time-dependent fluctuation of the packing density and hence give rise to the deterioration of the quality of the product. Various large-scale powder processing technologies designed to better handle powders in feeding through hoppers, for example those which purposely induce the vibration of the bed of solids, could give rise to such segregation of the particles.

The segregation index values given by Eq. (7) for the case of density-matched spheres with  $\epsilon=0.20$  and  $V_c=0.8$  were found to be 0.79 and 0.71 for  $\alpha=7$  and 20, respectively. On the basis of these segregation parameter values, it was expected that for both cases the larger particles will tend to rise to the top. Also, as  $\alpha$  increases the segregation index decreases, which means that separation of the mixture will be more pronounced, as indeed is observed experimentally.

So far the discussion has concentrated on spherical particles. However most industrial materials consist of nonspherical particles. Milewski [13] studied experimentally the packing of rods and spheres and determined that, for rods, as the aspect ratio increases the  $\phi_{\max}$  decreases. Debbas and Rumpf [5] studied packed beds with irregularly shaped particles. They found that the finer nonspherical particles segregate to the bottom gradually.

The results of the experiments conducted with melamine powder following the same procedures as those of glass spheres are shown in Fig. 7. The cumulative plots of particle size vs. volume fraction for each section of the cylinder are shown. All three sections contain comparable amounts of particles with diameters less than 20  $\mu\text{m}$ . In the 20 to 40  $\mu\text{m}$  radius range, the distributions of the top and middle portions of the cylinder are similar, whereas the bottom contains fewer particles which are in this size range. The top section contains a significant quantity of particles with equivalent diameters greater than 70  $\mu\text{m}$ , as shown in Fig. 7.

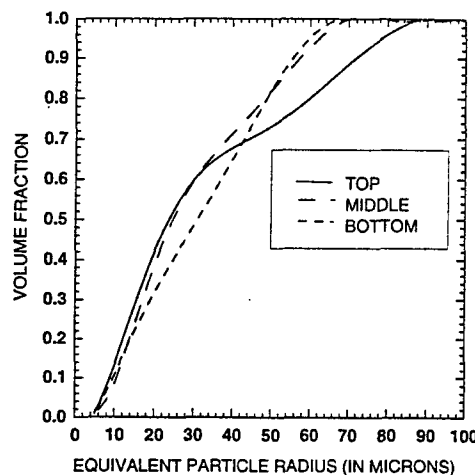


Fig. 7. Particle size distribution of melamine powder found at various locations of the cylinder.

The top section of the cylinder consists of a large portion of small particles (60% by volume under 30  $\mu\text{m}$ ) and a significant proportion of large particles (20% by volume over 60  $\mu\text{m}$ ). The large amount of small particles in the top section may be attributed to the elutriation segregation mechanism [14], which occurs principally due to the displacement of air. During pouring of the particles into the column, the velocity of the displaced air may equal or exceed the terminal fall velocity of the particles. A cloud of fine particles eventually settles and forms a layer at the top of the column. With vibration, this creates a dusting effect at the top of the column. On the other hand, the increase in the large size particles in this section indicates that the asymmetric particles also segregate according to particle size in a manner similar to that observed with spherical particles. Overall, the packing fraction determined for the melamine powder was only 0.5, reflecting the difficulty of achieving high packing density values with particles which exhibit aspect ratios greater than one.

## 5. Conclusions

The validity of theory of Ouchiyama and Tanaka [6-8] in predicting the packing density of spherical, noncohesive particles is further demonstrated with spherical particles consisting of bimodal and multimodal particle size distributions. However, it is also demonstrated that experimental techniques aiming to determine the packing density of powders are themselves subject to segregation effects.

The segregation of spherical glass and melamine particles according to size generated a significant variation in the volume fractions of the smaller and large spheres in a cylindrical column subjected to axial vi-

AUTHOR	EDITOR	MASTERCOPY	pages
QUERIES	CORRECTION	Vol. No.	pp.
Only typographical correction will be accepted at this stage.			

ELCOM3 PTESTD2862

08-09-94 11:25:12

bration. For both spherical and nonspherical particles, the top of the column contained a significant portion of the larger particles as well as a sizable portion of the smallest particles. This behavior is linked to segregation of particles according to size, on the basis of the downward movement of smaller particles and elutriation segregation of the smallest particles due to their entrainment in air. Overall, these results again illustrate the importance of the minimization of conditions which could lead to particle segregation during large-scale processing of powdery materials.

#### Acknowledgements

This study was made possible by a contract from the PBMA as managed by ONR under contract number N00014-90-J-4019. We are grateful for this support. The views expressed in this paper are those of the authors and not the government.

#### List of symbols

$D_a$	average diameter of the particles
$D_i$	diameter of the $i$ th particle
$f_i$	number fraction of the $i$ th component
$S$	segregation index
$V_c$	volume fraction of large particles
$V_i$	volume fraction of the $i$ th component

#### Greek letters

$\alpha$	ratio of diameters of spheres (large to small)
$\beta$	parameter given by Eq. (2)
$\epsilon$	porosity

$\rho$	density
$\phi$	packing fraction
$\phi_{\max}$	maximum packing fraction
$\phi_{\text{mo}}$	maximum packing fraction of uniform spheres
$\phi_m$	maximum packing fraction given by Eq. (6)

#### References

- [1] A.E.R. Westman and H.R. Hugill, *J. Am. Ceram. Soc.*, **13** (1930) 767.
- [2] C.C. Furnas, *Ind. Eng. Chem.*, **23** (1931) 1052.
- [3] G.D. Scott, *Nature*, **10** (1960) 908.
- [4] R.K. McGarry, *J. Am. Ceram. Soc.*, **44** (1961) 513.
- [5] S. Debbas and H. Rumpf, *Chem. Eng. Sci.*, **21** (1966) 583.
- [6] N. Ouchiya and T. Tanaka, *Ind. Eng. Chem. Fundam.*, **19** (1980) 338.
- [7] N. Ouchiya and T. Tanaka, *Ind. Eng. Chem. Fundam.*, **20** (1981) 66.
- [8] N. Ouchiya and T. Tanaka, *Ind. Eng. Chem. Fundam.*, **23** (1984) 490.
- [9] R.K. Gupta and S.G. Seshadri, *J. Rheol.*, **30** (1986) 503.
- [10] J.S. Chong, E.B. Christiansen and A.D. Baer, *J. Appl. Polym. Sci.*, **15** (1971) 2007.
- [11] A.J. Poslinski, M.E. Ryan, R.K. Gupta, S.G. Seshadri and F.J. Frechette, *J. Rheol.*, **32** (1988) 751.
- [12] W.M. Visscher and M. Bolsterli, *Nature*, **239** (1972) 504.
- [13] J.V. Milewski, *Ind. Eng. Chem. Prod. Res. Dev.*, **17** (1978) 363.
- [14] W.C. Williams, in M. Rhodes (ed.), *Principles of Powder Technology*, Wiley, New York, 1990.
- [15] K.T. O'Brien, A. Rosato and Y. Lan, *SPE ANTEC Technical Papers*, (1990) 64.
- [16] T. Matsumoto, N. Hidaka, H. Takenouchi and S. Morooka, *Powder Technol.*, **68** (1991) 131.
- [17] L.M. Popplewell and M. Peleg, *Powder Technol.*, **67** (1991) 21.
- [18] M. Alonso, M. Satoh and K. Miyamoto, *Powder Technol.*, **68** (1991) 145.
- [19] N. Harnby, in N.G. Stanley-Wood (ed.), *Enlargement and Compaction of Particulate Solids*, Butterworths, Cambridge, UK, 1983.



US005277058A

## United States Patent [19]

Kalyon et al.

[11] Patent Number: 5,277,058

[45] Date of Patent: Jan. 11, 1994

## [54] ADJUSTABLE GAP RHEOMETER

[76] Inventors: Dilhan M. Kalyon, 529 N. St., Teaneck, 07666; Halit S. Gokturk, 209 Second St., Apt. 2R, Hoboken, both of N.J. 07030

[21] Appl. No.: 979,747

[22] Filed: Nov. 23, 1992

[51] Int. Cl.<sup>5</sup> ..... G01N 11/04

[52] U.S. Cl. ..... 73/54.11; 73/54.14

[58] Field of Search ..... 73/54.11, 54.14; 33/813, 823, 828, 824, 825, 826; 269/86, 119, 140, 216, 320

## [56] References Cited

## U.S. PATENT DOCUMENTS

1,554,899 9/1925 Vick ..... 269/86  
1,850,178 3/1932 McChesney ..... 269/140  
2,661,540 12/1953 Dulligan ..... 33/544.5  
2,835,040 5/1958 D'Elia ..... 33/813  
3,046,666 7/1962 Mesich ..... 33/813  
3,203,225 8/1965 Sieglaff et al. ..... 73/54.14  
3,270,553 9/1966 Ballman et al. ..... 73/54.14  
3,595,305 7/1971 Welty et al. ..... 73/54.11  
4,313,339 2/1982 Nichols et al. ..... 73/54.14  
4,335,516 6/1982 Edelstein ..... 33/813  
4,448,736 5/1984 Emery et al. ..... 425/145  
4,466,274 8/1984 Starr, Jr. ..... 73/54.01  
4,587,837 5/1986 Newbould ..... 73/54.04  
4,817,416 4/1989 Blanch et al. ..... 73/54.04

## OTHER PUBLICATIONS

Chang Dae Han, "Measurement of the Rheological Properties of Polymer Melts with Slit Rheometer",

Journal of Applied Polymer Science, vol. 15, pp. 2567-2577 (1971).

Paul W. Springer, Robert S. Brokey and R. Emerson Lynn, "Development of an Extrusion Rheometer Suitable for On-Line Rheological Measurements", Polymer Engineering and Science, vol. 15, No. 8, pp. 583-587 (Aug. 1975).

Primary Examiner—Robert J. Warden

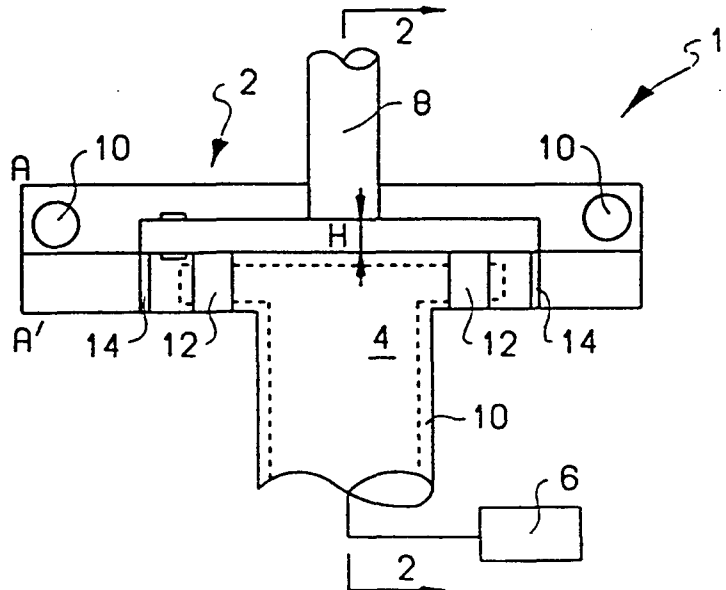
Assistant Examiner—Theresa A. Trembley

Attorney, Agent, or Firm—Pennie & Edmonds

## [57] ABSTRACT

An improved rheometer of the present invention includes an adjustable gap through which a flowing system is forced. The inner cavity dimension of the gap is variable so as to give a user of the rheometer an ability to vary the separation gap and the length over diameter ratio. This, in turn, allows the user to determine the shear rate and shear stress along the wall of the cavity for varying deformation rates. Thus, the shear viscosity of the flowing system can be characterized for non-Newtonian systems without varying the volumetric flow rate. One of the preferred embodiments of the adjustable gap rheometer is a slit rheometer in which the flowing system is forced through a slit having generally more length than width and more width than gap. The slit rheometer is made adjustable by holding the body of the rheometer stationary while moving an adjustable wall which forms one of the sides of the slit. Another preferred embodiment of the adjustable gap rheometer includes two concentric portions comprising a mandrel portion and a bushing portion. Axial movement of one of the portions relative to the other varies the separation between the components.

18 Claims, 2 Drawing Sheets



## ADJUSTABLE GAP RHEOMETER

## BACKGROUND OF THE INVENTION

This invention relates to the characterization of a flowing system such as a fluid or a mixture of fluids or a mixture of liquids with gases and/or solids by determining the rheological properties of the flowing system. More particularly, the invention relates to an improved rheometer having an adjustable inner cavity dimension so that properties of the flowing system are easily varied and the flowing system can be characterized without altering the volumetric flow rate of the flowing system.

Generally, rheometers operate by forcing the flowing system to be characterized through a die at a constant volumetric flow rate and determining specific properties of the flowing system such as the shear rate and shear stress of the flowing system at the wall of the die in order to determine the shear viscosity. These properties are characteristic of the flow and deformation behavior of the flowing system. The shear viscosity, in particular, is the most important rheological property.

The flow and deformation behavior are related to primary characteristics of the flowing system such as molecular weight, molecular weight distribution, extent of chain branching in polymer melts, degree of cure or conversion in a reacting system, and various microstructural distributions in multiphase systems. The microstructural distributions include the size distributions, locations and orientations of solid components in the flow, the concentration, shape, surface and size distributions of liquid droplets and the content and size distributions of gaseous components. Thus, characterization of the rheological behavior of a flowing system provides information on the structure of the system.

The rheological properties of the flowing system are characterized by employing material functions such as wall shear stress versus deformation rate at the wall or shear viscosity versus deformation rate determined on the basis of well-defined steady flows.

Rheometers of the prior art include capillary or slit rheometers. They operate by forcing the flowing system through a capillary die or a slit die at a specified volumetric flow rate with a drive mechanism such as a piston or a gear mechanism.

Because shear viscosity of a non-Newtonian flowing system is dependent on the deformation rate of the system, characterization of a non-Newtonian flowing system requires that shear rate and shear stress values be determined at multiple deformation rates to determine the viscosity over the deformation range of interest. Conventional rheometers achieve this by altering the volumetric flow rate into the rheometer. In this way, properties of the flowing system such as the shear rate and shear stress values are altered, and it is possible to determine the viscosity of the particular flowing system of interest over the deformation range of interest. However, altering the flow rate can change the structure and, hence, the rheological properties of the flowing system if a continuous process is used to deliver the flowing system to the rheometer. This distorts the results of the rheological study. Further, generating multiple flow rates requires equipment which is both cumbersome and expensive. Thus, a need exists for a rheometer which can determine the shear viscosity of non-

Newtonian flowing systems from a constant flow rate through the rheometer.

## SUMMARY OF THE INVENTION

An improved rheometer of the present invention includes an adjustable gap through which the flowing system is forced. The inner cavity dimension of the gap is variable so as to give a user of the rheometer an ability to vary the separation gap and the length over diameter ratio. This, in turn, allows the user to measure the shear rate and shear stress along the wall of the cavity for varying deformation rates. Thus, the shear viscosity of the flowing system can be determined for non-Newtonian systems without varying the volumetric flow rate.

One of the preferred embodiments of the adjustable gap rheometer is a slit rheometer. The slit rheometer comprises a gap through which the flowing system is forced which is shaped as a slit having generally more length than width and more width than gap. The slit rheometer is made adjustable by holding the body of the rheometer stationary while moving an adjustable wall which forms one of the sides of the slit. In this method, the gap dimension is made variable.

Another preferred embodiment of the adjustable gap rheometer includes two concentric portions comprising a mandrel portion and a bushing portion. Axial movement of one of the portions relative to the other varies the separation between the components. Thus, the gap between these portions through which the flowing system flows can be altered to create varying deformation rates of the flowing system, and the viscosity can be measured from measuring the shear stress of the flowing system for each deformation rate.

The advantages of the adjustable gap rheometer are many. First, the volumetric flow rate of the flowing system is maintained at a constant rate, thus eliminating the cost of expensive equipment required to alter the flow rate. Even more importantly, the constant flow rate maintains the microstructure of flowing systems that are sensitive to the thermo-mechanical history to which they are exposed during processing (especially multi-phase flowing systems) before they arrive at the separation gap of the rheometer. Thus, the rheological behavior of the flowing system is maintained during pre-gap processing, and the shear viscosity of the flowing system is measured with greater accuracy.

Another advantage of the adjustable gap rheometer is the ability to "structure" the material that flows through it by altering the deformation rates imposed on the flowing systems. Structuring the flowing material comprises altering the microstructural distributions of the components of the flowing system. The deformation rate imposed on the flowing system created by the particular gap through which the system flows alters the distribution of system components and hence, alters the microstructural distribution. Thus, by sending the flowing system through the adjustable gap rheometer, various microstructural features of the system can be determined for a particular flowing system. These features can be characterized by techniques such as computer aided tomography, magnetic resonance imaging, acoustic emission techniques, infrared imaging, and others. These microstructural features of the flowing system can later be used to create better flowing systems with improved microstructure, and, hence, better ultimate properties, to better understand the particular flowing system, or to help design better experiments which can

accommodate for the new microstructure distribution so as to more accurately characterize the rheological properties of the flowing system.

An additional advantage includes the ease with which the rheometer can be adjusted (as opposed to prior art techniques requiring a complete replacement or adjustment of the die upon stopping, and removal of the die of the rheometer at great expense and effort).

#### BRIEF DESCRIPTION OF THE FIGURES

These and other objects, features, elements and advantages of the invention will be more readily apparent from the following description of the invention in which:

FIG. 1 is a diagrammatic representation of one embodiment of an adjustable gap rheometer.

FIG. 2 is a cross-sectional view of the embodiment of the adjustable gap rheometer depicted in FIG. 1 taken at Section line 2-2.

FIG. 3 is a diagrammatic view of another embodiment of an adjustable gap rheometer.

#### DETAILED DESCRIPTION OF THE PREFERRED EMBODIMENT

A slit rheometer measures viscosity of a flowing system by measuring the apparent flowing system shear rate ( $\gamma$ ) as defined by

$$\gamma = \frac{6Q}{WH^2}$$

where  $Q$  is the volumetric flow rate,  $W$  is the width of the slit, and  $H$  is the separation gap of the slit; and the shear stress ( $\tau_w$ ) of the flowing system at the wall of the slit as defined by

$$\tau_w = \frac{H\Delta P}{2L}$$

where  $L$  is the slit length over which the shear stress is measured, and  $\Delta P$  is the pressure drop over the slit length of the fully developed flow. Known corrections which are dependent on the wall shear stress versus apparent shear rate behavior of the flowing system are applied to the apparent shear rate to determine true shear rate at the wall,  $\gamma_w$ . Shear viscosity ( $\eta$ ) is defined by

$$\eta = \frac{\tau_w}{\gamma_w}$$

To determine the shear viscosity of a non-Newtonian fluid (i.e., a fluid wherein the shear viscosity is dependent on the deformation rate), the shear viscosity values must be determined at multiple deformation rates.

To alter the deformation rate of the flowing system, the separation gap,  $H$ , of the rheometer is altered. Thus, with a constant flow rate,  $Q$ , the shear viscosity,  $\eta$ , of the flowing system can be determined. The rheometer of the invention can characterize the complete rheological behavior of the flowing system over a broad range of deformation rates, typically 0.01 to 5,000  $s^{-1}$ .

FIGS. 1 and 2 depict an embodiment of an adjustable gap rheometer of the invention comprising a slit die rheometer. The rheometer 1 comprises a stationary section 2 and a moveable section 4 which form the rheometer slit therebetween. In the alternative, the stationary and moveable sections can be reversed to

achieve the same result. The moveable section has two-directional vertical movement and is driven by a stepper motor 6 or by other such mechanisms. Movement of the moveable section 4 increases or decreases the separation gap,  $H$ , of the rheometer, thus varying the deformation rate of the flowing system.

The rheometer includes a plurality of flow property measuring devices 8 such as pressure transducers, shear stress transducers, optical windows and temperature thermocouples. Heating/cooling circulation channels 10 through which heat transfer fluids can be circulated at a desired temperature and rate maintain a constant temperature in the system. Cartridge type heaters 12 are also provided for better temperature control. Gasket elements 14 positioned adjacent the moveable section 4 prevent the fluid from leaking out of the slit. These gasket elements can comprise a sealing material such as a teflon material to create a strong seal.

The flowing system to be tested is forced through the rheometer at a constant flow rate,  $Q$ , which is generated by a continuous processor 16 such as a single or twin screw extruder or kneader which is run at the starved mode. The processor is externally controlled by feeding it at a constant flow rate. Alternatively, the flow rate could be generated by a gear pump installed in-line to feed the flowing system at a constant flow rate.

The constant volumetric flow rate is essential to maintain a constant processing history of the flow, which, in turn, maintains a constant microstructural distribution in the flowing system prior to entry into the separation gap. The microstructural distribution in the flow will determine the response of the flowing system to a deformation rate, and will, therefore, affect the accurate characterization of the rheological properties of the flowing system. Thus, the ability to run the rheometer at a constant flow rate will produce a more accurate determination of the shear viscosity.

Another embodiment of the invention is depicted in FIG. 3. The rheometer 20 comprises a concentric arrangement of a mandrel 22 and bushing 24. The structure 20 comprises a mandrel 22 which is tapered at a specific incline angle (for example 8°), which is moveable within a die bushing 24, which can be tapered at a generally larger angle than the mandrel (for example 9°). Alternatively, the mandrel taper angle and bushing taper angle could be the same. The taper angles may be maintained at less than 10° to preserve the simplified flow field which allows for better characterization of rheological properties. Between the mandrel 22 and the bushing 24 is a separation gap,  $H$ , through which a flowing system is forced in order to determine its rheological properties. Stepper motor 26, is coupled to the mandrel 22 via a rod or screw 28 to provide two-directional linear displacement of the mandrel. This, in turn, increases or decreases the separation gap,  $H$ , between the mandrel 22 and bushing 24 by an amount which is a function of the difference between the taper angles of the mandrel and the bushing, and the linear displacement of the mandrel within the bushing.

As in the case of the embodiment of FIG. 1, changing the separation gap,  $H$ , of the rheometer of FIG. 3 will change the wall deformation rate of the flowing system and thus will allow for the calculation of the shear viscosity of a non-Newtonian fluid. The rheometer includes a plurality of flow property measuring devices including pressure transducers, shear stress transducers, temperature thermocouples and optical windows, all

14. The adjustable gap rheometer according to claim 1 further comprising heaters to control the temperature of the flowing system.

15. The adjustable gap rheometer according to claim 1 wherein said means for moving at least part of said first or second portion comprise a stepper motor.

16. The adjustable gap rheometer according to claim 1 further providing means for maintaining a constant volumetric flow rate in the flowing system.

17. An improved method of performing rheological studies comprising:

providing an adjustable gap rheometer comprising a first portion and a second portion which form a separation gap therebetween;

adjusting said separation gap of said adjustable gap rheometer by moving at least a part of said first portion, said second portion or both portions of said adjustable gap rheometer; moving a flowing system having a constant volumetric flow rate through said separation gap; and measuring properties of the flowing system so as to characterize the flowing system at that predetermined separation gap.

18. The method according to claim 17 further comprising determining the structure of the flowing system by utilizing microstructural characterization techniques including computer aided tomography, magnetic resonance imaging, acoustic emission techniques and infrared imaging.

20

25

30

35

40

45

50

55

60

65

Chem. Eng. Comm. 1993, Vol. 122, pp. 127-150  
Reprints available directly from the publisher.  
Photocopying permitted by license only.  
© 1993 Gordon and Breach Science Publishers S.A.  
Printed in the United States of America

## EXTRUSION AND LUBRICATION FLOWS OF VISCOPLASTIC FLUIDS WITH WALL SLIP

ALDENYI LAWAL, DILFIAN M. KALYON<sup>†</sup> and ULKU YILMAZER<sup>‡</sup>

Department of Chemistry and Chemical Engineering  
Stevens Institute of Technology  
Castle Point on the Hudson  
Hoboken, NJ 07030, USA

(Received May 22, 1992; in final form November 18, 1992)

The simplest model flow which approximates the extrusion (shallow screw channels) and lubrication flow is the steady, laminar flow occurring between two infinitely long parallel plates i.e., the generalized plane Couette flow. Here we develop an analytical model of the generalized plane Couette flow of viscoplastic fluids. The deformation and flow behavior of viscoplastic fluids can be realistically represented with the Herschel-Bulkley constitutive equation, which we have utilized as the basis for the development of our analytical model. Furthermore, as also demonstrated here, the deformation behavior of viscoplastic fluids is generally complicated by the presence of wall slip at solid walls, which occurs as a function of the wall shear stress. The wall slip versus the wall shear stress behavior of viscoplastic fluids can be experimentally characterized using viscometric flows, including steady torsional and capillary flows. Thus determined Navier's wall slip coefficient can then be utilized in modeling of processing flows. In our analytical model of the generalized plane Couette flow of viscoplastic fluids the Navier's wall slip boundary condition was included. This model should be an important engineering tool, which provides design expressions for the extrusion and lubrication flows of viscoplastic fluids, with or without wall slip occurring at the walls.

KEY WORDS Extrusion lubrication flow viscoplastic slip.

### INTRODUCTION

Continuous processing technologies, including single screw and twin screw extruders and continuous kneaders, rely on drag induced flow and pressurization where the fluid is conveyed and pressurized by the action of at least one moving surface. Such screw pumps are generally theoretically analyzed by simplifying the geometry and considering the unwound flow channel to consist of an infinite plate sliding on the top of a stationary screw (McKelvey, 1962; Tadmor and Klein, 1970). For cases where the ratio of the depth of the channel (distance between the root of the screw and the barrel),  $H$ , divided by the width of the channel (distance between the flights in the transverse to flow direction),  $W$ , i.e.,  $H/W$  ratio is small, the extrusion flow can be represented by the idealized model flow of drag

<sup>†</sup>To whom correspondence should be addressed.

<sup>‡</sup>Present address: Middle East Technical University, Ankara, Turkey.

yield stress as well as shear thinning behavior. Furthermore, the deformation of viscoplastic fluids is generally subject to the occurrence of wall slip. Thus, a realistic model for the processing of viscoplastic fluids should include the facility to incorporate the wall slip boundary condition at the wall when wall slip exists.

The occurrence of wall slip, i.e., a relative velocity between the fluid velocity at the wall and the wall velocity is well documented for a variety of fluids, materials of construction and geometries. Wall slip in pressure flows, especially the capillary flow, has received considerable attention both theoretically and experimentally. Mooney's investigation of slip in capillary flow dates back to 1931 (Mooney, 1931). Various mechanisms for wall slip at the liquid-solid boundary layer region, including a number of apparent slip mechanisms, were reviewed by Silliman and Scriven (Silliman and Scriven, 1980), who also provided the full vector form of Navier's slip condition. Reviews of wall slip were published by White (White, 1973) and Petrie and Denn (Petrie and Denn, 1976) in conjunction with flow instabilities. The theoretical and experimental consequences of wall slip phenomenon were reviewed by Schowalter (Schowalter, 1988), who also emphasized the interplay between fluid mechanics and material science in affecting wall slip. In single screw extrusion analysis, Kalyon and co-workers have used the wall slip velocity versus wall shear stress behavior characterized from viscometric flows as the boundary condition in the mathematical modeling of single screw extruders (Ji, Gotsis and Kalyon, 1990). However, the finite element method based simulation methodology is too complicated for general adaptation and use. Menning (Menning, 1981) and Meijer and Verbraak (Meijer and Verbraak, 1988) have investigated the single screw extrusion of Newtonian fluids subject to wall slip.

The wall slip behavior of melts of commodity resins, including polyethylenes (Blyer and Hart, 1970; Ramamurthy, 1986a; Ramamurthy, 1986b; Kaliak and Denn, 1987; Atwood and Schowalter, 1989; Hatzikiriakos and Dealy, 1991; Chen, Kalyon and Bayramli, 1992) and poly (vinyl chloride) (Ramamurthy, 1986b), are extensively studied and generally related to flow instabilities. Studies related to the wall slip behavior of aqueous and organic polymer solutions in capillary and duct flows are also available (Kraynik and Schowalter, 1981; Cohen and Metzner, 1985; Müller-Mohnsen, Weiss and Tippe, 1990). Although these documented cases of wall slip are important, the most spectacular effects of wall slip are encountered with gels and concentrated suspensions (Jiang, Young and Metzner, 1986; Windhab and Gleisner, 1984; Boersma *et al.*, 1991; Yilmazer and Kalyon, 1989; Kalyon *et al.*, 1993), which are also generally viscoplastic. With gels and concentrated suspensions, the wall slip may dominate the flow behavior (Jiang, Young and Metzner, 1986; Yilmazer and Kalyon, 1989; Kalyon *et al.*, 1993). With the capillary flows of such materials, the volume flow rate may be entirely due to slip at the wall (with an apparent slip mechanism) over broad ranges of wall shear stress below (Kalyon *et al.*, 1993) or above a critical wall shear stress (Jiang, Young and Metzner, 1986; Yilmazer and Kalyon, 1989), depending on whether the suspension is shear thinning or shear thickening (Kalyon *et al.*, 1993).

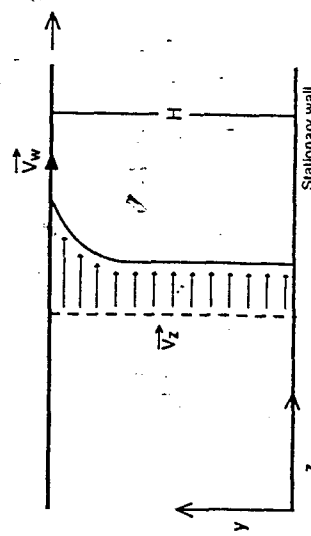
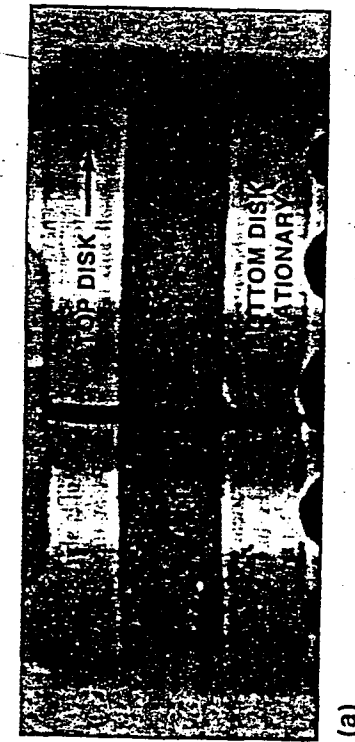


FIGURE 1 Generalized plane Couette flow.

induced pressurization between two parallel plates i.e., Generalized Plane Couette flow.

For shallow screws, the generalized Plane Couette flow provides an excellent model flow to predict functional dependences of the velocity profile of the fluid being processed and design expressions, principally the volumetric flow rate versus pressurization rate relationship, on geometry, fluid rheology and operating conditions. Under conditions where curvature effects are negligible this flow also represents the lubrication flow occurring in between two concentric cylinders, one of which is rotating. The plane Couette flow is depicted in Figure 1, where the fluid is confined in the space between two flat horizontal surfaces of infinite dimensions that are separated by a distance,  $H$ . The lower surface at  $y = 0$  is stationary, while the upper surface at  $y = H$  is moving in the  $+z$  direction in its own plane with a uniform velocity,  $v_w$ . In addition, there is a constant pressure gradient,  $\partial P / \partial z$ , acting in the  $z$ -direction. The pressure gradient arises under cases where there is a restriction such as a die or reversely configured screw elements following the channel. The pressure gradient may be acting in the same or opposite direction to the motion of the upper surface. The incompressible fluid is flowing under steady-state, laminar and isothermal flow conditions.

This classical problem in conjunction with the no-slip boundary condition, has been solved earlier for Newtonian fluids (Schlichting, 1955), and the "Power-Law" model of Ostwald-de Waele by Rotem and Shinnar (Rotem and Shinnar, 1961), Glyde and Holmes-Walker (Glyde and Holmes-Walker, 1962), Kroesser and Middleman (Kroesser and Middleman, 1965), and Bird and co-workers (Flumerfelt *et al.*, 1969). The solution for the Bingham plastic model fluid, again with the no-slip boundary condition, is also available (Tichy, 1991). The use of the Bingham plastic model to represent the behavior of viscoplastic fluid is very restrictive. The Bingham fluid behaves like a Newtonian fluid at shear stress values which exceed the yield stress of the fluid. However, most viscoplastic fluids exhibit shear thinning above the yield stress value. This necessitates the use of a constitutive equation such as the Herschel-Bulkley fluid, which incorporates a



(a)



(b)

FIGURE 2 Marker technique demonstrating wall slip of viscoplastic fluids.

#### Demonstration of Wall Slip in Drag Induced Flows

The typical wall slip behavior of a concentrated suspension is shown in Figure 2, under the drag flow imposed by a viscometric flow i.e., steady torsional flow in between two parallel disks. In this flow the top disk is rotating at an angular velocity and the bottom disk is stationary. A concentrated suspension consisting of sixty three percent by volume glass spheres, incorporated into an acrylonitrile terminated polybutadiene, fills the gap between the two plates.

A straight line marker is placed on the free surface of the suspension and on the edges of the plates before the onset of deformation, as shown in Figure 2a. This marker line is monitored and recorded during the deformation of the suspension at an apparent shear rate of  $0.01 \text{ s}^{-1}$ . As shown in Figure 2b, upon the onset of deformation, discontinuities appear at the suspension/wall interfaces for both disks i.e., at both the top and bottom. These discontinuities are indicative of wall slip and, upon optical measurement, can be utilized to determine wall slip versus the shear stress relationship (Kalyon *et al.*, 1993).

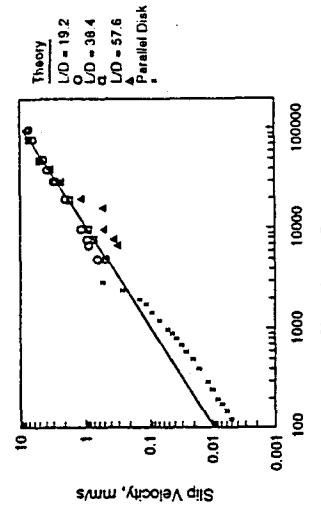
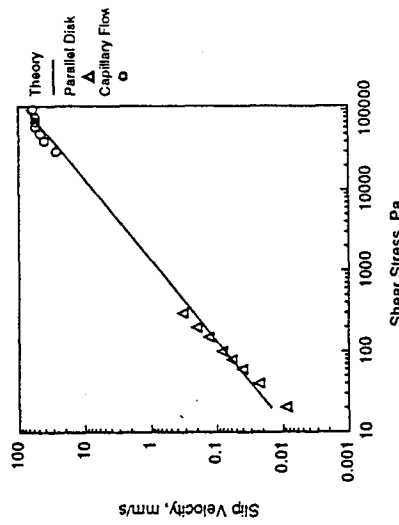


FIGURE 3 Slip velocity versus wall shear stress behavior of two concentrated suspensions; top figure 77 percent by volume ammonium sulfate and aluminum in acrylonitrile terminated polybutadiene and bottom figure 60 percent by volume ammonium sulfate and aluminum in hydroxyl terminated polybutadiene (reproduced from Kalyon *et al.*, 1993, and Yilmazer and Kalyon, 1989).

$L/D$ , ratios. The wall slip velocity,  $U_z$ , values depend on the wall shear stress,  $\tau_w$  as:

$$U_z = \beta \tau_w \quad (1)$$

where  $\beta$  is Navier's slip coefficient. The values of  $\beta$  are  $9.2 \times 10^{-5}$  mm/(Pa-s) and  $7.4 \times 10^{-4}$  mm/Pa-s for these suspensions, which contain 60 and 77 percent by volume solids, respectively. Kalyon and co-workers (Chen, Kalyon and Bayramli, 1992) have shown that the Navier's slip coefficient,  $\beta$ , depends on the materials of construction and surface roughness of the walls of the viscometer used to characterize wall slip, for even relatively simple materials like linear low density polyethylene. It is the capability to determine the slip velocity versus wall shear stress behavior under well defined conditions, which renders the following analysis relevant.

Here we present the complete analytical solution for the generalized Couette flow of viscoplastic fluids, following the Herschel–Bulky constitutive equation, subject to the Navier's wall slip condition. The special cases of this analytical solution also provide the solutions for various other generalized Newtonian fluids, including the Power Law fluid of Ostwald-de Waele, the Bingham plastic fluid and the Newtonian fluid. The analysis can be utilized to gain a first order understanding of the pressurization of viscoplastic fluids in shallow screw pumps and lubrication flows and the role played by wall slip.

## ANALYSIS

The generalized plane Couette flow of incompressible fluids results in the following  $z$ -component of the equation of motion (compressive stresses are positive):

$$-\frac{\partial \tau_{yz}}{\partial y} = \frac{dP}{dz} \quad (2)$$

where  $P$  is pressure, and  $\tau_{yz}$  is the shearing stress. For this one-dimensional flow, the Herschel–Bulky model is given by:

$$\tau_{yz} = -m \left| \frac{du_z}{dy} \right|^{n-1} \frac{du_z}{dy} \pm \tau_0 \quad |\tau_{yz}| \geq \tau_0 \quad (3a)$$

$$\frac{du_z}{dy} = 0 \quad |\tau_{yz}| \leq \tau_0 \quad (3b)$$

Here  $m$  and  $n$  are material parameters and  $\tau_0$  is the yield stress, i.e., a critical value of the stress magnitude below which viscoplastic materials do not flow. Bird et al. (Bird, Dai and Yarusso, 1983) have compiled a list of about forty materials which exhibit viscoplastic behavior and the Herschel–Bulky model is widely

used to represent their behavior. Here, the minus sign is to be used when  $\tau_{yz} < 0$ . At stress magnitudes  $|\tau_{yz}|$  which are less than the yield stress, only the rigid body motion, i.e. plug flow, is possible.

Defining the following dimensionless variables:

$$u_z = \frac{v_z}{v_w} \quad (4a)$$

$$\xi = \frac{y}{H} \quad (4b)$$

$$\Lambda = \left( \frac{H^{n+1}}{m v_w^n} \right) \frac{dP}{dz} \quad (4c)$$

Equation (2) becomes:

$$\frac{d}{d\xi} \left( \left| \frac{du_z}{d\xi} \right|^{n-1} \frac{du_z}{d\xi} \right) = \Lambda \quad (4d)$$

Equation (4d) is applicable only in the deformation region and is replaced by the rigid body translation requirement, Eq. (3b), in the plug region, whenever it exists. The volume flow rate  $Q$  is given by:

$$Q = \int_0^W \int_0^H v_z(y) dx dy = W H v_w \Omega \quad (5a)$$

where the dimensionless volume flow rate,  $\Omega$ , is:

$$\Omega = \int_0^1 u_z d\xi \quad (5b)$$

and  $W$  is the width of the slit in the  $x$ -direction.

## Navier Slip Condition

In two-dimensional flow configurations, the expression for slip at the wall when modelled by the Navier slip condition is of the form (Silliman and Scriven, 1980):

$$\mathbf{t} \cdot (\mathbf{v} - \mathbf{v}_s) = \beta \mathbf{n} \cdot \boldsymbol{\tau} \quad (6)$$

where  $\mathbf{t}$  is the unit tangent vector to the surface,  $\mathbf{n}$  the unit outward normal and  $\beta$  is the slip parameter. The limits for  $\beta = \infty$  and  $\beta = 0$  give perfect slip and no slip conditions respectively.  $\mathbf{v}$  and  $\mathbf{v}_s$  are the velocity vectors of the fluid and the solid surface respectively, and  $\boldsymbol{\tau}$  is the total stress tensor. In general,  $\beta$  may depend on

the invariants of the stress tensor, but here it is assumed to be a material constant. This does not impose any serious limitation on the results, as experimental data generally confirm this to be the case (Yilmazer and Kalyon, 1989).

The slip velocity is defined as the difference between the fluid velocity and the velocity of the solid surface. When Eq. (6) is applied to the two surfaces, one obtains in dimensionless form:

$$u_{sr} = \left( \frac{\beta}{v_w} \right) \tau_{yr}(H) \quad (7a)$$

$$u_{sb} = - \left( \frac{\beta}{v_w} \right) \tau_{yr}(0) \quad (7b)$$

where  $u_{sr}$  and  $u_{sb}$  represent the slip velocity values at the top and bottom surfaces, respectively. Using Eq. (2), the slip velocities are related through:

$$u_{sr} = \alpha - u_{sb} \quad (8a)$$

and

$$\alpha = \frac{\beta H \left( - \frac{dP}{dz} \right)}{v_w} \quad (8b)$$

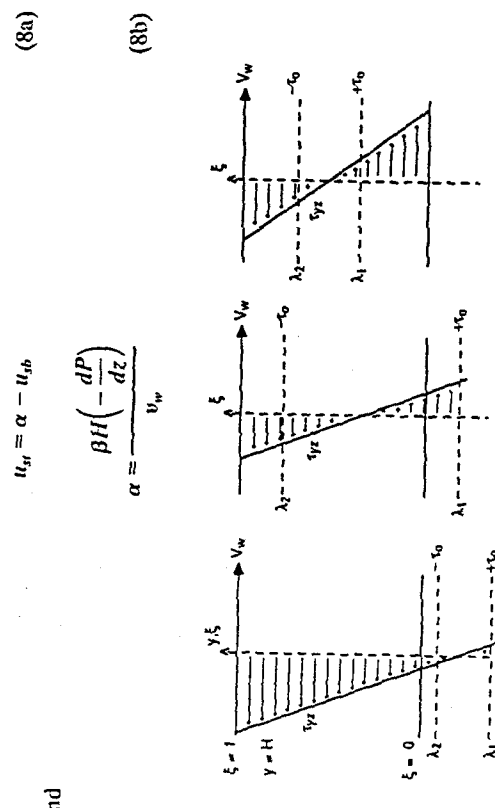


FIGURE 4 Schematic representation of the velocity and shear stress profiles for three cases with  $dP/dz > 0$ .

This does not impose any serious limitation on the results, as experimental data generally confirm this to be the case (Yilmazer and Kalyon, 1989).

The slip velocity is defined as the difference between the fluid velocity and the velocity of the solid surface. When Eq. (6) is applied to the two surfaces, one obtains in dimensionless form:

$$u_{sr} = \left( \frac{\beta}{v_w} \right) \tau_{yr}(H) \quad (7a)$$

$$u_{sb} = - \left( \frac{\beta}{v_w} \right) \tau_{yr}(0) \quad (7b)$$

where  $u_{sr}$  and  $u_{sb}$  represent the slip velocity values at the top and bottom surfaces, respectively. Using Eq. (2), the slip velocities are related through:

$$u_{sr} = \alpha - u_{sb} \quad (8a)$$

and

$$\alpha = \frac{\beta H \left( - \frac{dP}{dz} \right)}{v_w} \quad (8b)$$

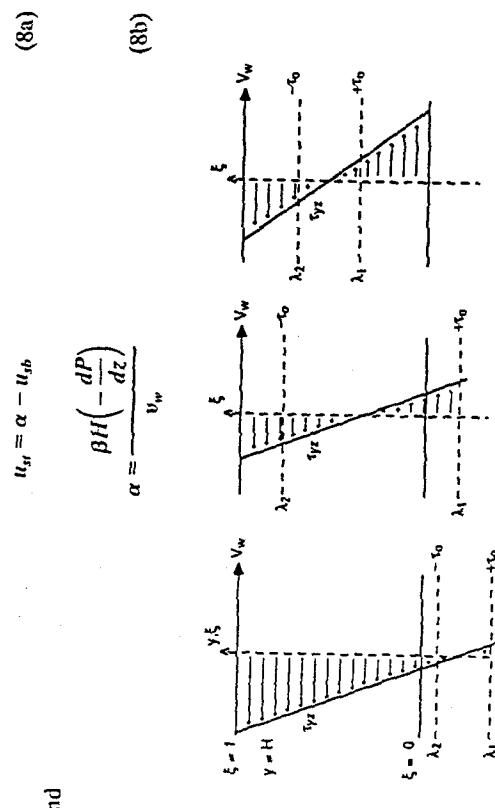


FIGURE 5 Schematic representation of the velocity and shear stress profiles for three cases with  $dP/dz < 0$ .  
 (a) Case 1  
 (b) Case 2  
 (c) Case 3

Three distinct cases, with their stress and velocity profiles as depicted in Figures 4 and 5, are possible depending on the values of the parameters of the problem. These cases are:

- Case 1: No plug flow region; which occurs when the stress magnitude is greater than the yield stress in the entire flow domain, as depicted in Figure 4a and 5a.
- Case 2: Plug flow occurs with the non-deforming plug attached to the bottom surface for positive pressure gradient as shown in Figure 4b, and attached to the top surface as shown in Figure 5b for negative pressure gradient.
- Case 3: Plug flow occurs, with the rigid core sandwiched in between two deforming zones as shown in Figure 4c and 5c for positive and negative pressure gradients, respectively. This case will be referred to as the "floating plug" region.

Designating the lower interface between the deformation region and the plug flow region by  $\lambda_1$ , and the upper interface by  $\lambda_2$ , the analysis for the three cases for positive and negative values of  $\Lambda$  can be carried out as shown in the Appendix. The results are summarized in the Appendix and Table 1.

TABLE I

Case 1—no plug region ( $\Lambda < 0$ )	
$u_z = \frac{(-\Lambda)^s}{(s+1)} \lambda_1^{s+1} - \frac{(-\Lambda)^s}{(s+1)} (\lambda_1 - \xi)^{s+1} + \kappa + \alpha \lambda_1$	$0 \leq \xi \leq 1$
$\Omega = \frac{(-\Lambda)^s}{(s+1)(s+2)} [(\lambda_1 - 1)^{s+2} - \lambda_1^{s+2}] + \frac{(-\Lambda)^s}{(s+1)} \lambda_1^{s+1} + \kappa + \alpha \lambda_1$	
where $\lambda_1$ is given by:	
$\frac{(-\Lambda)^s}{(s+1)} (\lambda_1 - 1)^{s+1} - \frac{(-\Lambda)^s}{(s+1)} \lambda_1^{s+1} - 2\kappa - \alpha(2\lambda_1 - 1) + 1 = 0$	(28a)
$\frac{(-\Lambda)^s}{(s+1)} \lambda_1^{s+1} - \frac{(-\Lambda)^s}{(s+1)} (\lambda_1 - \xi)^{s+1} + \kappa + \alpha \lambda_1$	$0 \leq \xi \leq \lambda_1$
$u_z = \frac{(-\Lambda)^s}{(s+1)} \lambda_1^{s+1} + \kappa + \alpha \lambda_1$	$\lambda_1 \leq \xi \leq 1$
$\Omega = \frac{(-\Lambda)^s}{(s+1)} \lambda_1^{s+1} - \frac{(-\Lambda)^s}{(s+1)(s+2)} \lambda_1^{s+2} + \kappa + \alpha \lambda_1$	
where $\lambda_1$ is given by:	
$1 - 2\kappa - \alpha(2\lambda_1 - 1) - \frac{(-\Lambda)^s}{(s+1)} \lambda_1^{s+1} = 0$	(29a)
Case 2—plug attached to the top surface ( $\Lambda < 0$ )	
$u_z = \frac{(-\Lambda)^s}{(s+1)} \lambda_1^{s+1} - \frac{(-\Lambda)^s}{(s+1)} (\lambda_1 - \xi)^{s+1} + \kappa + \alpha \lambda_1$	$0 \leq \xi \leq \lambda_1$
$u_z = \frac{(-\Lambda)^s}{(s+1)} \lambda_1^{s+1} + \kappa + \alpha \lambda_1$	$\lambda_1 \leq \xi \leq 1$
$\Omega = \frac{(-\Lambda)^s}{(s+1)} \lambda_1^{s+1} - \frac{(-\Lambda)^s}{(s+1)(s+2)} \lambda_1^{s+2} + \kappa + \alpha \lambda_1$	
where $\lambda_1$ is given by:	
$1 - 2\kappa - \alpha(2\lambda_1 - 1) - \frac{(-\Lambda)^s}{(s+1)} \lambda_1^{s+1} = 0$	(29b)
Case 3—floating plug region ( $\Lambda < 0$ )	
$u_z = \frac{(-\Lambda)^s}{(s+1)} \lambda_1^{s+1} - \frac{(-\Lambda)^s}{(s+1)} (\lambda_1 - \xi)^{s+1} + \kappa + \alpha \lambda_1$	$0 \leq \xi \leq \lambda_1$
$u_z = 1 + \frac{(-\Lambda)^s}{(s+1)} (1 - \lambda_2)^{s+1} - \kappa - \alpha(\lambda_1 - 1)$	$\lambda_1 \leq \xi \leq \lambda_2$
$u_z = \frac{(-\Lambda)^s}{(s+1)} (1 - \lambda_2)^{s+1} - \frac{(-\Lambda)^s}{(s+1)} (\xi - \lambda_2)^{s+1} - \kappa - \alpha(\lambda_1 - 1) + 1$	$\lambda_2 \leq \xi \leq 1$
$\Omega = \frac{(-\Lambda)^s}{(s+1)} (1 - \lambda_2)^{s+1} - \frac{(-\Lambda)^s}{(s+1)(s+2)} [(1 - \lambda_2)^{s+2} + \lambda_1^{s+2}] - \kappa - \alpha(\lambda_1 - 1) + 1$	
where $\lambda_2$ and $\lambda_1$ are related through:	
$\lambda_2 - \lambda_1 = \frac{-2\tau_0}{H \frac{dP}{dz}}$	(30e)

$$\alpha = \frac{\beta H(-dP/dz)}{v_w}, \quad \kappa = \beta \tau_0/v_w \quad \text{and} \quad \Lambda = \left( \frac{H^{n+1}}{m_w^n} \right) \frac{dP}{dz}$$

Here, we will illustrate the solution with a small number of case studies. Typical velocity profiles for small positive value of  $\Lambda = 0.1$  with the shear sensitivity index,  $n = 0.5$  and three values of  $\alpha$  are shown in Figure 8. For the values of  $|\alpha|$  at 0.1 and 0.25, the velocity profiles approximate the plug flow of the viscoplastic fluid with equal wall slip velocities at the top and bottom drag surfaces. This flow behavior is characteristic of many viscoplastic fluids. In Figure 9, the steady

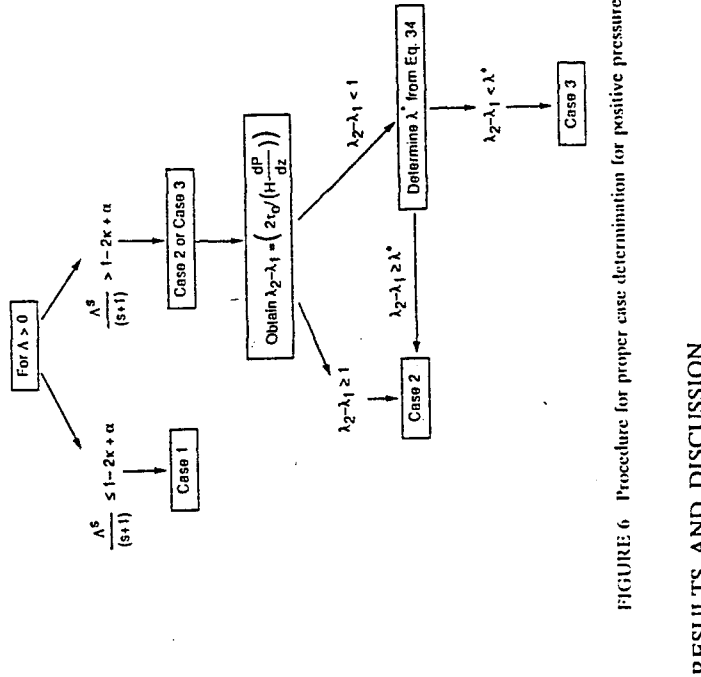


FIGURE 6 Procedure for proper case determination for positive pressure gradient.

## RESULTS AND DISCUSSION

With the rheological behavior, processing and operating conditions known, the procedure schematically illustrated in Figures 6 and 7 can be implemented in the selection of the appropriate case among the three possible cases. This requires the solution of the corresponding non-linear equations for the values of the extremum locations,  $\lambda_1$ ,  $\lambda_2$  and  $\lambda^*$ , which can be accomplished by using the standard Newton-Raphson's technique. The determination of the velocity profiles and the calculation of the volume flow rate then follow, using the equations summarized in the Appendix and Table I.

It is not possible to present comprehensive results, which cover all possible dimensionless parameters,  $\Lambda$ ,  $\kappa$  and  $\alpha$ , defined as

$$\lambda_2 - \lambda_1 = \frac{-2\tau_0}{H \frac{dP}{dz}}$$

and  $\lambda_1$  is obtainable from:

$$1 - \frac{(-\Lambda)^s}{(s+1)} \lambda_1^{s+1} - 2\kappa - \alpha(2\lambda_1 - 1) + \frac{(-\Lambda)^s}{(s+1)} (1 - \lambda_1 - 2\kappa/\alpha)^{s+1} = 0 \quad (30f)$$

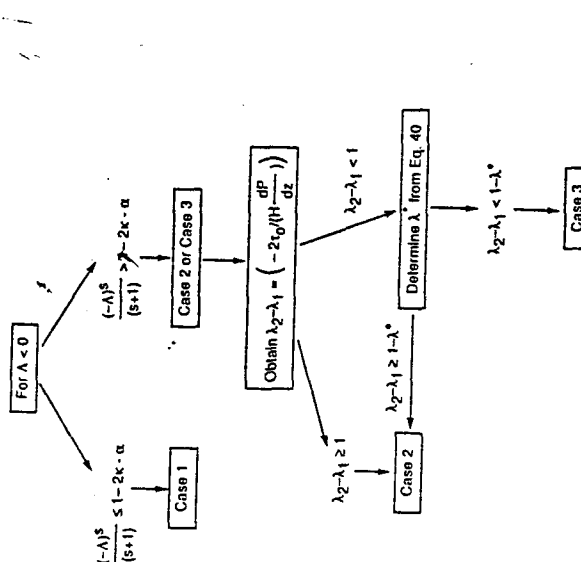


FIGURE 7 Procedure for proper case determination for negative pressure gradient.

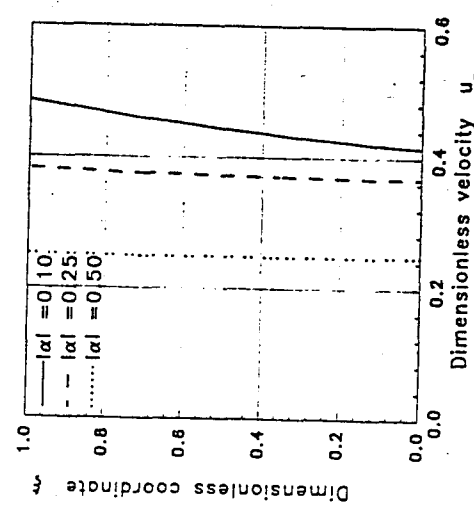
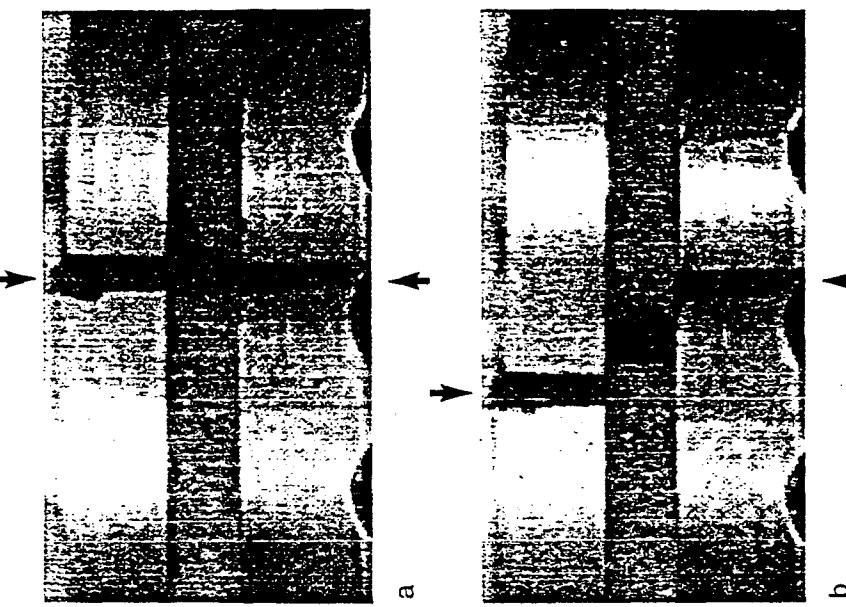
FIGURE 8 Typical velocity profiles for Case 1, corresponding to  $\lambda = 0.1$ ,  $n = 0.5$  and  $\kappa = 0.20$  as a function of  $|\alpha|$ .

FIGURE 9 The steady torsional flow of a suspension which exhibits plug flow with wall slip velocities at top and bottom disk surfaces.

torsional flow behavior of a viscoplastic suspension of sixty three percent by volume of glass spheres in acrylonitrile terminated polybutadiene is shown. As indicated through the straight line marker incorporated before the onset of the deformation introduced through the angular rotation of the top disk, the suspension exhibits only wall slip and does not deform, i.e., exhibits a plug flow with equal wall slip velocities at the top and bottom plate surfaces. Thus, this experimentally observed behavior is similar to the velocity profiles depicted in Figure 8.

As the value of  $|\alpha|$  is decreased, a small deformation rate is introduced into the viscoplastic fluid as is typical of Case 1. The fluid velocity increases monotonically

from a minimum at the bottom stationary surface to a maximum at the moving surface with the slip velocities as indicated in the figure. As shown for  $|\alpha| = 0.1$ , the slip velocity magnitudes are about 0.41 at the bottom surface and about 0.49 at the top surface. The small deformation rate introduced with significant wall slip velocities is reminiscent of the steady torsional flow of the suspension sample, the deformation of which is depicted earlier in Figure 2.

As  $\Lambda$  increases for the same shear sensitivity parameter,  $n = 0.5$ , Case 2 is reached with the plug region attached to the bottom surface as shown in Figure 10. The magnitude of the slip velocity at the bottom surface increases with decreasing  $|\alpha|$ , while that at the top surface increases with increasing  $|\alpha|$  value. A negative velocity value for the plug may be obtained, as shown for  $|\alpha| = 0.80$ .

The typical effects of the parameter  $\alpha$  on the volumetric flow rate-pressure gradient relationships for the viscoplastic i.e., Herschel-Bulkley fluid are shown in Figure 11 for the same value of parameter,  $n = 0.5$ , which governs the sensitivity of the fluid to the deformation rate. Both cases involving positive and negative pressurization rate ( $dP/dz$  greater and less than zero, respectively) are included in Figure 11. For positive pressurization rate, the critical value of the dimensionless pressure gradient,  $|\Lambda|$ , at which the volumetric flow rate commences to drop, increases with decreasing value of  $|\alpha|$ . Such results can be employed to assess the effects introduced by wall slip, viscoplasticity, geometrical parameters and operating conditions on the design relationships, involving volumetric flow rates versus the pressurization rate. The utilities of the developed analytical model will be demonstrated further with the following case studies, involving realistic material parameters and dimensions of industrial scale extruders.

#### Case Studies

In Table II a realistic set of material parameters of a viscoplastic suspension and geometry and operating conditions arising from our own experimental extrusion studies are included. The rheological material parameters are those of a highly filled suspension involving 77 percent of volume solids incorporated into a hydroxyl terminated polybutadiene binder (Kalyon *et al.*, 1993). The geometrical parameters are those of an industrial scale single screw extruder.

a) *Effect of the yield stress* Let's assume that the required pressurization rate,  $dP/dz$ , in the single screw extruder is 15 MPa/m. With the geometry and material parameters given in Table II, and a yield stress value of 83,800 Pa the dimensionless parameters become:

$$\Lambda = 2, \quad \kappa = 0.2, \quad \text{and} \quad |\alpha| = 0.25$$

As will be seen from Figure 11, the corresponding dimensionless volumetric flow rate,  $\Omega$ , is 0.21 (95 kg/hour). If the yield stress,  $\tau_0$ , is ignored in this analysis i.e.,  $\tau_0$  is assumed zero, with the dimensionless parameter,  $\kappa$ , becoming equal to zero, the dimensionless volumetric flow rate,  $\Omega$ , becomes 0.13. Thus, the ignoring of

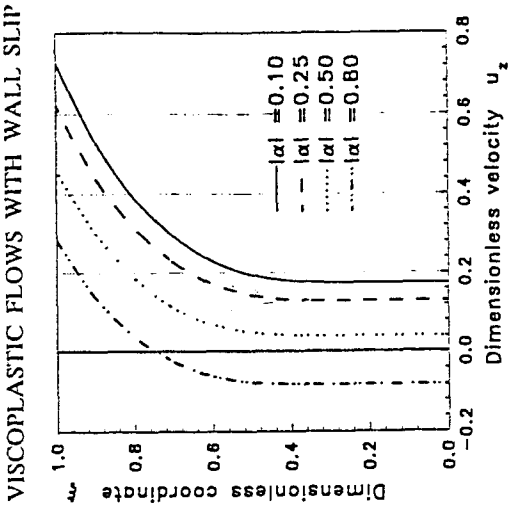


FIGURE 10 Typical velocity profiles for Case 2, corresponding to  $\Lambda = 2.0$ ,  $n = 0.5$  and  $\kappa = 0.2$ .  
 The viscosity of the fluid would have introduced a significant error in the calculation of the volumetric flow rate, at which the desired pressurization rate  $dP/dz$  of 15 MPa/m can be achieved.  
 The effect of the value of the yield stress of the fluid on the volumetric flow rate,  $\Omega$ , which can be achieved at a higher pressurization rate of 30 MPa/m, is

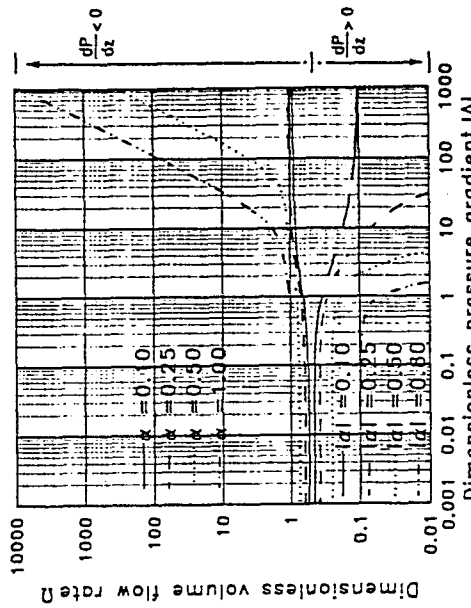


FIGURE 11 Typical volume flow rate versus pressure gradient for  $n = 0.5$  and  $\kappa = 0.2$ .

TABLE II

The geometry, operating conditions and material parameters used in the case study

Material Parameters
Herschel-Bulkley Fluid (Equations 1a and 3b)
Shear rate sensitivity parameter, $n = 0.5$
$m = 7,400 \text{ Pa-s}^{0.5}$
Navier's Wall Slip Coefficient, $= 7.4 \times 10^{-7} \text{ m}/(\text{Pa-s})$ (from Figure 3)
Density = $2,100 \text{ kg/m}^3$
Channel Dimensions
Channel Depth, $H = 0.007 \text{ m}$
Channel width, $W = 0.028 \text{ m}$
Operating Conditions
Linear Screw velocity = $0.3 \text{ m/s}$

shown in Figure 12. At small values of the yield stress (keeping everything else constant), the volumetric flow rates are negative, suggesting that the pressurization rate of the viscoplastic fluid desired,  $30 \text{ MPa/m}$ , can not be achieved under these operating conditions. As the yield stress value increases over  $10 \text{ KPa}$ ,

## VISCOPLASTIC FLOWS WITH WALL SLIP

143

positive volumetric flow rates are possible. For yield stress values greater than  $50 \text{ KPa}$ , the volumetric flow rate reaches a constant value and becomes insensitive to the value of the yield stress.

Overall, the increased volumetric flow rate at constant pressurization (or conversely, increased pressurization rate at constant volumetric flow rate) with increasing yield stress value of the fluid is associated with the increased shear viscosity of the fluid. It is interesting to note that as the suspension becomes more solid-like, its pressurization capability increases. In the limit, the pressurization rate associated with a deformable solid bed, being conveyed in plasticating extrusion process is very high, where an exponential increase in pressure with distance is observed (Darnell and Mol, 1956; Tadmor and Broyer, 1972; Kalyon and Hallouch, 1986).

b) *Effect of wall slip* With the channel dimensions, operating conditions and material parameters of the Herschel-Bulkley fluid given in Table II and with a yield stress value,  $\tau_0$ , of  $6,500 \text{ Pa}$  the dimensionless parameters are:

$$\Lambda = 2, \quad \kappa = 0.02, \quad |\alpha| = 0.25$$

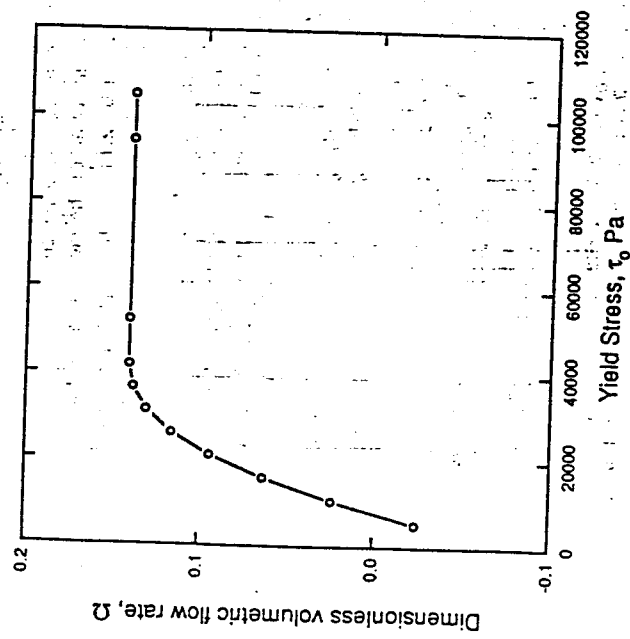


FIGURE 12 Effect of the yield stress value of the viscoplastic fluid on pressurization in the channel with  $\Lambda = 4$  and  $\beta = \kappa = \alpha = 0$  (for the no-slip condition).

Dimensionless volumetric flow rate,  $Q$

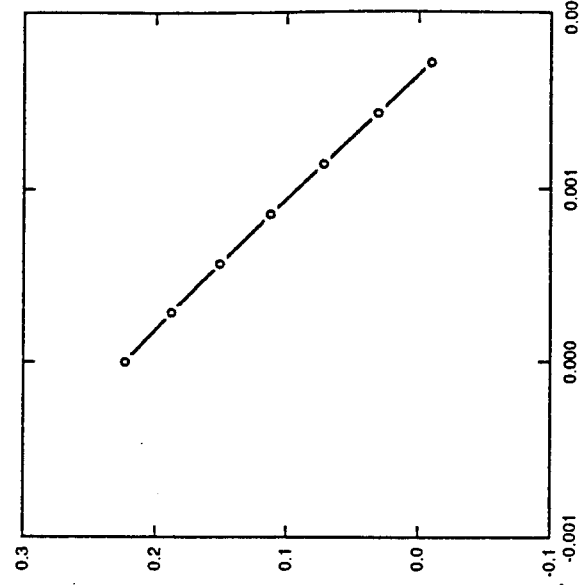


FIGURE 13 Effect of Navier's wall slip parameter on volumetric flow rate with  $\kappa = 0$ ,  $\Lambda = 2$  and  $dP/dz = 15 \text{ MPa/m}$ .

Dimensionless volumetric flow rate,  $Q$

which generates, upon the solution of Eqs. (20-27) for Case 3, a dimensionless volumetric flow rate,  $\Omega$ , of 0.14 (63 kg/hour). For this case if the presence of the wall slip is ignored, i.e., the Navier's wall slip coefficient,  $\beta$ , is taken as zero, the dimensionless parameters  $\kappa$  and  $\alpha$  become equal to zero and the resulting dimensionless volumetric flow rate,  $\Omega$ , becomes 0.22 (100 kg/hour). Thus, for this case, not considering the occurrence of slip condition at the wall results in the overprediction of the volumetric flow rate by about 60 percent.

The effect of Navier's wall slip coefficient,  $\beta$ , on the development of the pressurization capability in extrusion and lubrication flows is shown in Figure 13. As the wall slip coefficient,  $\beta$ , increases, the volumetric flow rate,  $\Omega$ , which corresponds to a pressurization rate of 15 MPa/m, decreases precipitously. Above a slip coefficient,  $\beta$ , of  $1.5 \times 10^{-3}$  mm/(Pa-s), the volumetric flow rates are negative, suggesting that it is not possible to achieve the desired pressurization rate of 15 MPa/m, even at very small production rates. These results emphasize how critical it is to incorporate wall slip behavior into the analysis of processing flows for materials which exhibit wall slip. The results also indicate how good engineering, including proper selections of the materials of construction and surface roughness of the processor or operating conditions, to alter wall slip behavior, can be useful in favorably affecting production rates in continuous processing flows.

#### ACKNOWLEDGEMENTS

The funding for this project was provided by the Department of the Navy, Office of the Chief of Naval Research. We are grateful for this support. The views expressed are those of the authors and not the Government of the U.S. and no official endorsement should be inferred.

#### NOMENCLATURE

$g$	acceleration due to gravity
$h$	distance above a reference equipotential gravity plane
$H$	distance of separation between the two parallel surfaces
$m$	consistency index in the shear viscosity function of Herschel-Bulkley fluid
$n$	rheological constant describing sensitivity of shear viscosity to deformation rate
$n$	unit normal vector
$p$	pressure
$P$	$p \rho gh$
$Q$	volume rate of flow
$s$	defined as $1/n$

$\epsilon$	unit tangent vector to a surface
$u_x$	dimensionless slip velocity at the bottom surface
$u_y$	dimensionless slip velocity at the top surface
$u_z$	dimensionless local fluid velocity in $z$ -direction
$v$	fluid velocity vector
$v_x$	velocity vector of solid wall
$v_w$	uniform velocity of the moving surface, i.e., wall velocity
$v_z$	fluid velocity in $z$ -direction
$W$	width of slit in the $x$ -direction
$x, y, z$	rectangular coordinates

#### Greek Letters

$\alpha$	dimensionless parameter $= \frac{\beta H(-dP/dz)}{v_w}$
$\beta$	slip coefficient
$\kappa$	dimensionless parameter $= \beta \tau_0 / v_w$
$\lambda_1$	lower interface between the deformation region and the plug region
$\lambda_2$	upper interface between the deformation region and the plug region
$\lambda^*$	limit on the thickness of the plug region
$\Lambda$	dimensionless pressure gradient $= \left( \frac{H^{n+1}}{m v_w^n} \right) \frac{dP}{dz}$
$\pi$	total stress tensor
$\Omega$	dimensionless volume flow rate
$\rho$	density
$\tau_0$	yield stress
$\tau_{yz}$	component of stress tensor
$\xi$	dimensionless coordinate in $y$ -direction

#### REFERENCES

Atwood, B.T., and Schowaller, W.R., *Rheol. Acta*, **28**, 134 (1989).  
 Bird, R.B., Dai, G.C., and Vansso, B.J., *Rev. in Chem. Eng.*, **1**, 1 (1983).  
 Blyler, Jr., L.L., and Hart, Jr., A.C., *Polym. Eng. Sci.*, **10**, 193 (1970).  
 Boersma, W.H., Buel, P.J.M., Laven, J., and Stein, H.N., *J. Rheol.*, **35**, 1093 (1991).  
 Chen, Y., Kalyon, D.M., and Bayramli, E., "Effects of Surface Roughness and the Chemical Structure of Materials of Construction on Wall Slip Behavior of Linear Low Density Polyethylene in Capillary Flow," accepted to appear in *J. Appl. Polym. Sci.* November 1992.  
 Chen, Y., Kalyon, D.M., and Bayramli, E., *Society of Plastics Engineers ANTEC Technical Papers*, **38**, 1747 (1992).  
 Cohen, Y., and Meizner, A.B., *J. Rheol.*, **29**, 67 (1985).

Darnell, W.H. and Mol, E.A., *Soc. Plast. Eng. J.*, **12**, 20 (1956).  
 Flumerfelt, R.W., Pierick, M.W., Cooper, S.L., and Bird, R.B., *EC Fundamentals*, **8**, 354 (1969).  
 Glyde, B.S., and Holmes-Walker, W.A., *International Plastic Engineering*, **2**, 338 (1962).  
 Hatzikirikos, S.G., and Dealy, J.M., *J. Rheol.*, **35**, 497 (1991).  
 Ji, Z., Gotsis, A., and Kalyon, D.M., *Society of Plastics Engineers ANTEC Technical Papers*, **36**, 160 (1990).  
 Jiang, T.Q., Young, A.C., and Metzner, A.B., *Rheol. Acta*, **25**, 397 (1986).  
 Kalyon, D.S., and Denn, M.M., *J. Rheol.*, **31**, 815 (1987).  
 Kalyon, D.M., and Hallouch, M., *Adv. Polym. Techn.*, **6**, 237 (1986).  
 Kalyon, D.M., Yaras, P., Aral, B., and Yilmazer, U., *J. Rheol.*, **37**, 35 (1993).  
 Kraynik, A.M., and Schowalter, W.R., *J. Rheol.*, **25**, 95 (1981).  
 Kroeser, F.W., and Middleman, S., *Polym. Eng. Sci.*, **5**, 230 (1965).  
 McKelvey, J.M., "Polymer Processing," John Wiley, New York, 1962.  
 Meijer, H.E.H., and Verbraak, C.P., *Polym. Eng. Sci.*, **28**, 758 (1988).  
 Menzies, G., *Kunstoffe*, **71**, 359 (1981).  
 Mooney, M., *J. Rheol.*, **2**, 210 (1931).  
 Müller-Mohrsen, H., Weiss, D., and Tippe, A., *J. Rheol.*, **34**, 223 (1990).  
 Petrie, C.J.S., and Denn, M.M., *AIChE J.*, **22**, 209 (1976).  
 Ramamurthy, A.V., "Advances in Polymer Technology," **6**, 489 (1986).  
 Rojmi, Z., and Shimar, R., *Chem. Eng. Sci.*, **15**, 130 (1961).  
 Schlichting, H., "Boundary Layer Theory," New York: McGraw Hill, 60-62, (1955).  
 Schowalter, W.R., *J. Non-Newtonian Fluid Mech.*, **29**, 25 (1988).  
 Silliman, W.J., and Tadmor, Z., *Comp. Phys.*, **34**, 287 (1980).  
 Tadmor, Z., and Shviv, L.E., *J. Comp. Phys.*, **12**, 378 (1972).  
 Tadmor, Z., and Klein, I., *Engineering Principles of Plasticating Extrusion*, Krieger, New York, 1970.  
 White, J.L., *Appl. Polym. Symp.*, **20**, 155 (1973).  
 Windhab, E., and Gleissle, W., "Proceedings of the 9th International Congress on Rheology," Mexico (1984).  
 Yilmazer, U., and Kalyon, D.M., *J. Rheol.*, **33**, 1197 (1989).

## APPENDIX

Case 1—no plug region ( $\Lambda > 0$ )

Since  $du_z/d\xi > 0$ , Eq. (4d) becomes:

$$\frac{d}{d\xi} \left( \frac{du_z}{d\xi} \right)^n = \Lambda \quad (9)$$

which can be integrated once to give:

$$\Lambda(\xi - \lambda_2) = \left( \frac{du_z}{d\xi} \right)^n \quad (10)$$

having made use of the condition that  $du_z/d\xi = 0$  at  $\xi = \lambda_2$ . Further integration of Eq. (10) subject to the boundary condition  $u_z(0) = u_{zb}$  gives:

$$u_z = \frac{\Lambda^s}{(s+1)} (\xi - \lambda_2)^{s+1} - \frac{\Lambda^s}{(s+1)} (-\lambda_2)^{s+1} + u_{zb} \quad (11)$$

where  $s = 1/n$ . If we apply the yield stress condition at  $\lambda_2$ ,  $u_{zb}$  is determined as:

$$u_{zb} = \kappa + \alpha \lambda_2 \quad (12)$$

where  $\kappa = \beta \tau_0 / u_w$ . For Bingham plastic materials, i.e.,  $n = 1$  and  $m$  as the plastic

## VISCOPLASTIC FLOWS WITH WALL SLIP

viscosity, the ratio  $(-\kappa\Lambda/\alpha)$  is the Bingham number. Equation (11) upon substitution for  $u_{zb}$  becomes:

$$u_z = \frac{\Lambda^s}{(s+1)} (\xi - \lambda_2)^{s+1} - \frac{\Lambda^s}{(s+1)} (-\lambda_2)^{s+1} + \kappa + \alpha \lambda_2 \quad (13)$$

The boundary condition at the top surface, i.e.  $u_z(1) = 1 + u_{sr}$  provides the relationship for  $\lambda_2$ , thus:

$$\frac{\Lambda^s}{(s+1)} (1 - \lambda_2)^{s+1} - \frac{\Lambda^s}{(s+1)} (-\lambda_2)^{s+1} + 2\kappa + \alpha(2\lambda_2 - 1) - 1 = 0 \quad (14)$$

where the expression for  $u_{sr}$  has been obtained by combining Eq. (8a) and Eq. (12). Integrating Eq. (13), the dimensionless volume flow rate is:

$$\Omega = \frac{\Lambda^s}{(s+1)(s+2)} [(1 - \lambda_2)^{s+2} - (-\lambda_2)^{s+2}] - \frac{\Lambda^s}{(s+1)} (-\lambda_2)^{s+1} + \kappa + \alpha \lambda_2 \quad (15)$$

Case 2—plug attached to the bottom surface ( $\Lambda > 0$ )

In the region where the fluid is being deformed, i.e.,  $\lambda_2 \leq \xi \leq 1$ , Eq. (10) applies. When Eq. (10) is integrated subject to the boundary condition at the top surface, the following velocity distribution is obtained:

$$u_z = \frac{\Lambda^s}{(s+1)} (\xi - \lambda_2)^{s+1} - \frac{\Lambda^s}{(s+1)} (1 - \lambda_2)^{s+1} - \kappa - \alpha(\lambda_2 - 1) + 1 \quad \text{for } \lambda_2 \leq \xi \leq 1 \quad (16)$$

In the plug region:

$$u_z = 1 - \frac{\Lambda^s}{(s+1)} (1 - \lambda_2)^{s+1} - \kappa - \alpha(\lambda_2 - 1) \quad 0 \leq \xi \leq \lambda_2 \quad (17)$$

To obtain the relationship for  $\lambda_2$ , we use the condition  $u_z(\lambda_2) = u_{zb}$  to give:

$$\frac{\Lambda^s}{(s+1)} (1 - \lambda_2)^{s+1} + 2\kappa + \alpha(2\lambda_2 - 1) - 1 = 0 \quad (18)$$

Finally, the dimensionless volume flow rate is:

$$\Omega = \frac{\Lambda^s}{(s+1)(s+2)} (1 - \lambda_2)^{s+2} - \frac{\Lambda^s}{(s+1)} (1 - \lambda_2)^{s+1} - \kappa - \alpha(\lambda_2 - 1) + 1 \quad (19)$$

Case 3—floating plug region ( $\Lambda > 0$ )

In the upper section, the solution to the velocity equation is as obtained for Case 2, i.e., Eq. (16), and therefore need not be repeated. However, in the lower section,  $du_z/d\xi < 0$ , and Eq. (4d) then becomes:

$$\frac{d}{d\xi} \left( -\frac{du_z}{d\xi} \right)^n = -\Lambda \quad (20)$$

Integrating Eq. (20) once and using the condition that  $du_z/d\xi = 0$  at  $\xi = \lambda_1$ , we

obtain:

$$\Lambda(\lambda_1 - \xi) = \left( -\frac{du_\xi}{d\xi} \right)^n \quad (21)$$

Further integration and the application of the bottom surface boundary condition, i.e.,  $u_\xi(0) = u_{\xi b}$  gives:

$$u_\xi = \frac{\Lambda^*}{(s+1)} (\lambda_1 - \xi)^{s+1} - \frac{\Lambda^*}{(s+1)} \lambda_1^{s+1} + \kappa + \alpha \lambda_2 \quad \text{for } 0 \leq \xi \leq \lambda_1 \quad (22)$$

In the plug region,

$$u_\xi = 1 - \frac{\Lambda^*}{(s+1)} (1 - \lambda_2)^{s+1} - \kappa - \alpha(\lambda_2 - 1) \quad \text{for } \lambda_1 \leq \xi \leq \lambda_2 \quad (23)$$

and since the plug region velocity is constant, the velocity of the fluid in the upper section at  $\xi = \lambda_2$  should be the same as the fluid velocity in the lower section at  $\xi = \lambda_1$ , hence:

$$1 - \frac{\Lambda^*}{(s+1)} (1 - \lambda_2)^{s+1} - \kappa - \alpha(\lambda_2 - 1) = -\frac{\Lambda^*}{(s+1)} \lambda_1^{s+1} + \kappa + \alpha \lambda_2 \quad (24)$$

The position of the lower interface of the plug region,  $\lambda_1$ , is related to the upper interface,  $\lambda_2$ , through:

$$\lambda_2 - \lambda_1 = \frac{2\tau_0}{H \frac{dP}{dz}} \quad (25)$$

Here the dimensionless ratio,  $2\tau_0/H(dP/dz)$  is equal to  $-2\kappa/\alpha$ , and it is assumed that the value of this ratio for zero wall slip coefficient  $\beta$  is to be obtained using L'Hopital's rule. Upon substitution, Eq. 24 becomes:

$$1 - \frac{\Lambda^*}{(s+1)} (1 - \lambda_2)^{s+1} - 2\kappa - \alpha(2\lambda_2 - 1) + \frac{\Lambda^*}{(s+1)} (\lambda_2 + 2\kappa/\alpha)^{s+1} = 0 \quad (26)$$

This is the required equation for the determination of  $\lambda_2$ , and  $\lambda_1$  can be subsequently recovered from Eq. (25). Integration of the velocity profile gives the dimensionless volume flow rate as:

$$\Omega = \frac{\Lambda^*}{(s+1)(s+2)} [\lambda_1^{s+2} + (1 - \lambda_2)^{s+2}] - \frac{\Lambda^*}{(s+1)} (1 - \lambda_2)^{s+1} - \kappa - \alpha(\lambda_2 - 1) + 1 \quad (27)$$

This completes the analysis for dynamic pressurization where  $dP/dz$  is positive, i.e.,  $\Lambda > 0$ . For a negative pressure gradient, the governing equations are different. The corresponding equations for  $\Lambda < 0$  are summarized in Table I.

Asymptotes for the special case of Bingham plastic fluids

For Bingham plastic materials ( $s = 1$ ), the volume flow rate reaches asymptotic values at small and large values of  $\Lambda$ . For Case 1 and small  $\Lambda$ , the asymptotic expression for the volume flow rate becomes:

$$\Omega = \frac{1}{2}[\alpha + 1] \quad (31a)$$

while for Case 3 and large values of  $\Lambda$ , the asymptotic expression for  $\Omega$  is:

$$\Omega = \Lambda \left[ -\frac{1}{12} \pm \frac{1}{4} \left( \frac{\kappa}{\alpha} \right)^3 \pm \frac{1}{4} \left( \frac{-\kappa}{\alpha} \right) \right] + 1 + \frac{\alpha}{2} \quad (31b)$$

where the minus sign applies for negative pressure gradient. The generalized plane Couette flow of a power-law fluid without wall slip is a special case of our more general analysis. The agreement with the results reported by Flumerfelt et al. (Flumerfelt et al., 1969) is excellent. The findings also agree with the results provided by Tichy (Tichy, 1991) for the plane Couette flow of a Bingham fluid, without wall slip to which our equations reduce for  $n = 1$  and  $\kappa$  and  $\alpha = 0$ .

Proper case determination

The first step in the procedure for determining the proper case is to determine if a plug flow region exists in the flow domain. Starting with  $\Lambda > 0$ , if we set  $\lambda_2$  to 0 in Eq. (14), it can be easily shown that the condition for a plug region not to exist is given by:

$$\frac{\Lambda^*}{(s+1)} \leq 1 - 2\kappa + \alpha \quad \text{for all } \lambda_2 - \lambda_1 \geq 0 \quad (\text{Case 1}) \quad (32)$$

and that the reverse holds when Eq. (32) is not satisfied, i.e.:

$$\frac{\Lambda^*}{(s+1)} > 1 - 2\kappa + \alpha \quad \text{for all } \lambda_2 - \lambda_1 \geq 0 \quad (\text{Cases 2 \& 3}) \quad (33)$$

To distinguish between Case 2 and Case 3, the value of  $\lambda^*$  which is a limit on the thickness of the core region is calculated. The expression for  $\lambda^*$  is obtainable from Eq. (24) by replacing  $\lambda_2$  by  $\lambda^*$  and setting  $\lambda_1$  to 0, hence:

$$\frac{\Lambda^*}{(s+1)} (1 - \lambda^*)^{s+1} + 2\kappa + \alpha(2\lambda^* - 1) - 1 = 0 \quad (34)$$

and Case 2 is obtained either if:

$$\lambda_2 - \lambda_1 = \left( \frac{2\tau_0}{H \frac{dP}{dz}} \right) \geq 1 \quad (35a)$$

$$\text{or} \quad \lambda_2 - \lambda_1 \geq \lambda^* \quad (35b)$$

while the condition for Case 3 is:

$$\lambda_2 - \lambda_1 < \lambda^* \quad (36)$$

For  $\Lambda < 0$ , the corresponding equations are:

Case 1

$$\frac{(-\Lambda)^s}{(s+1)} \leq 1 - 2\kappa - \alpha \quad \text{for all } \lambda_2 - \lambda_1 \geq 0 \quad (37)$$

Case 2

$$\frac{(-\Lambda)^s}{(s+1)} > 1 - 2\kappa - \alpha \quad (38)$$

$$\lambda_2 - \lambda_1 = \left( \frac{-2\tau_0}{H \frac{dP}{dz}} \right) \geq 1 \quad (39a)$$

or

$$\lambda_2 - \lambda_1 \geq 1 - \lambda^* \quad (39b)$$

where  $\lambda^*$  is calculated from:

$$1 - 2\kappa - \alpha(2\lambda^* - 1) - \frac{(-\Lambda)^s}{(s+1)}(\lambda^*)^{s+1} = 0 \quad (40)$$

Case 3

$$\frac{(-\Lambda)^s}{(s+1)} > 1 - 2\kappa - \alpha \quad (41)$$

$$\lambda_2 - \lambda_1 < 1 - \lambda^* \quad (42)$$

These conditions are schematically depicted in Fig. 6 and Fig. 7 for  $\Lambda$  greater than and less than zero, respectively.

## INTRODUCTION

For isolating a desired protein or an enzyme from a complex mixture, the two phase aqueous extraction technique offers the advantages of gentle environment, favourable processing time and easy scale-up (Albertsson (1985)). Recent technical advances on the polymer-salt and polymer-polymer phase systems have enhanced the chances for commercial exploitation of this technique on a large scale.

Conventional extraction equipment can be conveniently used for aqueous two phase systems. In our earlier communication Sawant *et al.* (1990), have reported some preliminary work on spray columns. The aim of present work is to investigate the effect of design (column diameter, column height and distributor design) and operating (dispersed phase velocity and physical properties) parameters on the dispersed phase hold-up and the volumetric mass transfer coefficient.

<sup>f</sup> To whom correspondence should be addressed.

## ENZYME MASS TRANSFER COEFFICIENT IN AQUEOUS TWO PHASE SYSTEMS: SPRAY EXTRACTION COLUMNS

P.A. PAWAR, K. ROSTAMI JAFARABAD, S.B. SAWANT<sup>f</sup> and  
J.B. JOSHI

Department of Chemical Technology  
University of Bombay  
Mumbai, Bombay-400 019, India

(Received January 24, 1992; in final form December 31, 1992)

Fractional dispersed phase hold-up and overall dispersed phase side mass transfer coefficients were measured in 34, 50, 70 and 95 mm i.d. spray columns using an aqueous two phase system. Sodium sulphate-polyethylene glycol (PEG) (4000)-water formed the aqueous two phase system and amyloglucosidase was used as a solute for the estimation of mass transfer coefficient.

The dispersed phase hold-up ( $\epsilon_D$ ) and volumetric dispersed phase side mass transfer coefficient ( $K_{D,1}$ ) both increased with increasing PEG-rich phase velocity. The  $\epsilon_D$  and  $K_{D,1}$  were found to be independent of the column diameter and column height above a certain critical value. An increase in the phase concentration of sodium sulphate and PEG was found to reduce  $\epsilon_D$  and  $K_{D,1}$ . Empirical and semi-empirical correlations for  $\epsilon_D$  and  $K_{D,1}$  have been developed.

**KEYWORDS** Mass transfer coefficients. Amyloglucosidase. Spray column. Two phase aqueous systems.